



HAL
open science

Afterslip and viscoelastic relaxation model inferred from the large-scale post-seismic deformation following the 2010Mw8.8 Maule earthquake (Chile)

Emilie Klein, L Fleitout, C Vigny, Jean-Didier Garaud

► **To cite this version:**

Emilie Klein, L Fleitout, C Vigny, Jean-Didier Garaud. Afterslip and viscoelastic relaxation model inferred from the large-scale post-seismic deformation following the 2010Mw8.8 Maule earthquake (Chile). *Geophysical Journal International*, 2016, 205, pp.1455 - 1472. 10.1093/gji/ggw086 . hal-03033640

HAL Id: hal-03033640

<https://hal.science/hal-03033640>

Submitted on 1 Dec 2020

HAL is a multi-disciplinary open access archive for the deposit and dissemination of scientific research documents, whether they are published or not. The documents may come from teaching and research institutions in France or abroad, or from public or private research centers.

L'archive ouverte pluridisciplinaire **HAL**, est destinée au dépôt et à la diffusion de documents scientifiques de niveau recherche, publiés ou non, émanant des établissements d'enseignement et de recherche français ou étrangers, des laboratoires publics ou privés.

Afterslip and viscoelastic relaxation model inferred from the large-scale post-seismic deformation following the 2010 M_w 8.8 Maule earthquake (Chile)

E. Klein,^{1,*} L. Fleitout,¹ C. Vigny¹ and J.D. Garaud²

¹Laboratoire de Géologie, ENS, UMR 8538, CNRS, Member of PSL-research University, 24 rue Lhomond, F-75231 Paris Cedex 05, France.

E-mail: klein@geologie.ens.fr

²Onera - The French Aerospace Lab, F-92322 Châtillon, France

Accepted 2016 February 29. Received 2016 February 10; in original form 2015 October 5

SUMMARY

Megathrust earthquakes of magnitude close to 9 are followed by large-scale (thousands of km) and long-lasting (decades), significant crustal and mantle deformation. This deformation can be observed at the surface and quantified with GPS measurements. Here we report on deformation observed during the 5 yr time span after the 2010 M_w 8.8 Maule Megathrust Earthquake (2010 February 27) over the whole South American continent. With the first 2 yr of those data, we use finite element modelling (FEM) to relate this deformation to slip on the plate interface and relaxation in the mantle, using a realistic layered Earth model and Burgers rheologies. Slip alone on the interface, even up to large depths, is unable to provide a satisfactory fit simultaneously to horizontal and vertical displacements. The horizontal deformation pattern requires relaxation both in the asthenosphere and in a low-viscosity channel along the deepest part of the plate interface and no additional low-viscosity wedge is required by the data. The vertical velocity pattern (intense and quick uplift over the Cordillera) is well fitted only when the channel extends deeper than 100 km. Additionally, viscoelastic relaxation alone cannot explain the characteristics and amplitude of displacements over the first 200 km from the trench and aseismic slip on the fault plane is needed. This aseismic slip on the interface generates stresses, which induce additional relaxation in the mantle. In the final model, all three components (relaxation due to the coseismic slip, aseismic slip on the fault plane and relaxation due to aseismic slip) are taken into account. Our best-fit model uses slip at shallow depths on the subduction interface decreasing as function of time and includes (i) an asthenosphere extending down to 200 km, with a steady-state Maxwell viscosity of 4.75×10^{18} Pa s; and (ii) a low-viscosity channel along the plate interface extending from depths of 55–135 km with viscosities below 10^{18} Pa s.

Key words: Time-series analysis; Satellite geodesy; Seismic cycle; Subduction zone processes; Rheology: mantle; South America.

1 INTRODUCTION

Post-seismic deformation can be explained by three different mechanisms, with different temporal and spatial scales: (i) poroelastic rebound (Jonsson *et al.* 2003), (ii) afterslip on the main rupture zone (Marone *et al.* 1991; Hsu *et al.* 2006; Chlieh *et al.* 2007), and (iii) viscoelastic relaxation (VER) in the mantle (Melosh & Raefsky 1983; Savage 1983; Thatcher & Rundle 1984). The occurrence of megathrust earthquakes during the last decade provided

unprecedented data set to better understand those mechanisms and a combination of at least two of those mechanisms is often invoked to reproduce the observed deformation pattern. 40 yr after the 1960 M_w 9.5 Valdivia earthquake (Chile) or the 1964 Alaska earthquake, trenchward motions are still observed on sites located 300–400 km away from the ruptured area. This indicates long-term stress relaxation in the mantle (Khazaradze *et al.* 2002; Suito & Freymueller 2009). For Chile, a viscoelastic finite element model suggesting a continental upper mantle with a viscosity of 2.5×10^{19} Pa s and an oceanic mantle with a viscosity of 10^{20} Pa s explain well the trenchward motion of inland sites as well as the uplift visible 200 km away from the trench (Hu *et al.* 2004). However, for both earthquakes, we lack data over the first years immediately after the events. These

*Now at: Institut Physique du Globe, UMR 7516, Université de Strasbourg/EOST, CNRS Strasbourg, France.

early data are crucial to discriminate between the different phenomena involved and constrain the mechanisms of post-seismic deformation. 6 yr after the M_w 9.2 Sumatra–Andaman earthquake, large-scale subsidence was reported all over Thailand with a rate of the order of 1 cm yr^{-1} and was attributed to post-seismic relaxation in the asthenosphere (Satirapod *et al.* 2013). 3 yr after the 2011 M_w 9.0 Tohoku earthquake, combinations of afterslip and viscoelastic relaxation (Diao *et al.* 2014; Sun & Wang 2015; Yamagiwa *et al.* 2015) or of poroelastic rebound and viscoelastic relaxation (Hu *et al.* 2014) are used to explain the post-seismic deformation occurring very close to the trench and detected by seafloor stations. The very dense available data set also allows to better study on one hand the effects of structural characteristics on the post-seismic response at the surface (Trubienko *et al.* 2014) and, on the other hand, interactions between different mechanisms, highlighting for example the overestimation of afterslip when using pure elastic models (Sun & Wang 2015).

Thanks to a better comprehension of the role of various rheological and geometrical parameters of the subduction zone detailed in (Trubienko *et al.* 2014), we focus here on the post-seismic deformation following the M_w 8.8 2010 Maule megathrust earthquake (February 27, Chile), developing the same methodology. This

earthquake produced a maximum of horizontal coseismic displacement of about 5 m at the coast, and detectable coseismic deformation across the continent up to Buenos Aires in Argentina, where 15 mm of coseismic displacement were recorded (Vigny *et al.* 2011). Though only the near-field deformation has been studied through time-variable afterslip models (Bedford *et al.* 2013), the Maule earthquake offers the unique advantage to have occurred at the border of the South American continent which is not covered by sea, unlike Tohoku or Aceh earthquakes for which large portions of the overriding plate cannot be monitored. Distinct patterns of the post-seismic deformation established over 150 sites spanning the whole continent, during the 5 yr following the earthquake (Fig. 1) allow to quantify the combination of afterslip and viscoelastic relaxation occurring in specific deep layers of the mantle. Since we are specifically looking at the large-scale and long-term deformation, meaning at the scale of the seismic cycle, we are not considering here poroelastic rebound, which produces small-scale deformation (Jonsson *et al.* 2003).

This study has two purposes. We first present the surface post-seismic pattern, measured using the Global Positioning System (GPS), over 5 yr following the Maule earthquake. Secondly, we propose a state-of-the-art method using an FE model combining

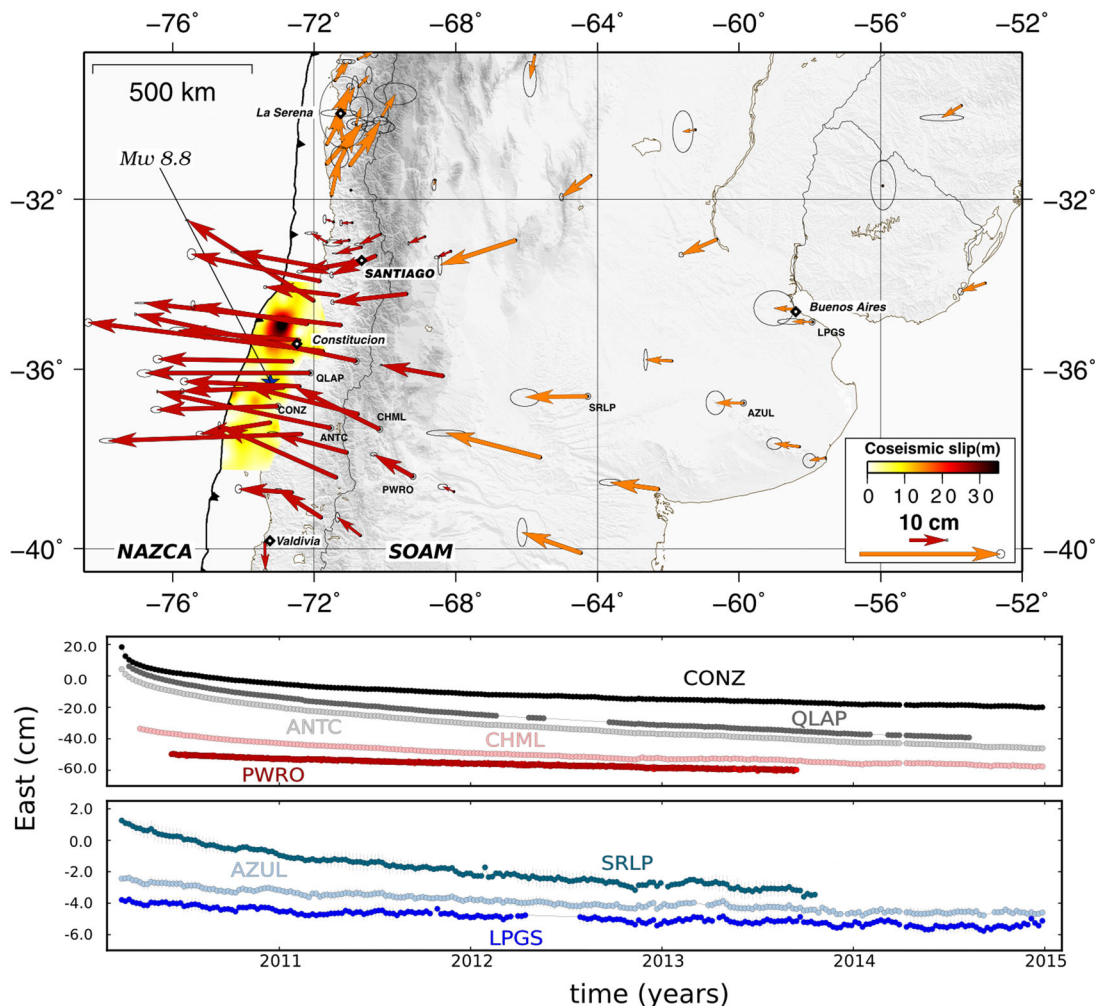


Figure 1. Top: horizontal cumulative displacements over 5 yr, in cm, (between 2010 and the end of 2014), corrected from the interseismic rates. Two different scales have been used depending on the amplitude. The coseismic slip distribution is the one inverted in this study (in m) and the blue star depicts the epicentre of the earthquake located by the National Sismological Center of Chile (CSN). Bottom: East component of GPS time-series of stations identified on the map, sorted by distance to the trench, as a function of time (cm).

viscoelastic relaxation and afterslip, which allows to deal with the additional component of relaxation generated by the aseismic slip on the fault plane. We then discuss the geometry of the subduction interface and the rheologies of the low-viscosity zones constrained using the first 2 yr of data.

Section 2 describes the GPS data processing, the analysis of time-series and finally the extracted post-seismic pattern on the whole continent. The finite element model set-up and modelling methodologies are described in Section 3. In Section 4, we report on different results, starting with our coseismic slip distribution. We then explore models of pure afterslip on one hand and of pure viscoelastic relaxation on the other hand, having previously detailed the impact on surface deformation of relaxation in the various low-viscosity areas through synthetic tests. The necessity of adding shallow afterslip is then discussed, along with its impact on surface deformation versus the impact of viscoelastic relaxation. In Section 5, we discuss several implications of our best fit model: the impact of using Burgers rheologies, the geometry and origin of low-viscosity areas, the possible existence of a cold and more rigid craton in Central Argentina and finally the implications of our model for longer time-scales. The model presented in this paper is constrained using the first 2 yr of GPS data. Though, having analysed 5 yr of data, we compare and discuss this model's prediction over those 5 yr and also at the scale of the seismic cycle.

2 DATA

The Maule region (32–37°S) was known as a mature seismic gap since it last ruptured in 1835 (Ruegg *et al.* 2009). There, the accumulation of deformation was monitored closely since the first GPS campaigns of 1996 (Ruegg *et al.* 2009). Also, several permanent stations were installed in the early 2000's. In the first weeks following the 2010 Maule earthquake, many new continuous GPS stations have been installed in and around the rupture area to complete the existent network. Today, more than 30 stations monitor very precisely the post-seismic deformation in the first 200 km from the trench. Previous studies have highlighted that post-seismic deformation following megathrust earthquakes are significant several thousands of kilometres away from the rupture zone (Satirapod *et al.* 2013; Trubienko *et al.* 2014). To monitor this continental scale deformation, we use a selection of about 100 stations spanning the South-American continent: in Chile (LIA MdB, IPOC, CANTO, CAP networks), in Argentina (RAMSAC network), Brazil (RBMC network) and IGS stations. Finally, we distinguish stations in three zones depending on their distance from the trench: near-field corresponding to the first 300 km from trench, mid-field: the area between 300 and 500 km, and far-field, the area more than 500 km away from the trench.

2.1 GPS data processing

We reduce 24 hr sessions to daily site positions using the GAMIT software (King & Bock 2000). The ionosphere-free combination is chosen, and ambiguities are fixed to integer values. We use precise orbits from the International GNSS Service for Geodynamics (IGS; Dow *et al.* 2009) and the phase centres of the antennae are described using IGS Tables. One tropospheric vertical delay parameter per station is estimated every 3 hr. The horizontal (resp. vertical) components of the calculated relative position vectors have repeatabilities of 1–3 (resp. 3–5) mm. We then produce weekly time-series using the GLOBK software (Herring *et al.* 2010). Because the deformation induced by the earthquake affects a very large area, a

'regional stabilization' approach (in which only continental stations are used to constrain the reference frame) is insufficient to provide a stable reference frame and the realization of a global reference frame is necessary. To do so, we combine our daily solutions with daily global H-files produced at SOPAC, using globally distributed IGS stations. We produce weekly coordinates, mapped into the ITRF 2008 (Altamimi *et al.* 2011) using a set of regional and global stations with well-known coordinates in the ITRF08 (Table S1 in the Supporting Information). Residuals are typically of the order of 3–5 mm, indicating the level of precision of the mapping in the ITRF. The weekly combination also considerably lowers the high-frequency noise (± 3 d) in the time-series.

2.2 Time-series analysis

Our modelling is based on the best possible fit to post-seismic trends. Therefore, the quality of the model relies on extracting the most precise and purest post-seismic signals from the observed deformation. The first step is to correctly quantify the pre-seismic signal, so that this signal can be removed from post-earthquake observations, yielding pure post-seismic deformations. North of 38°S, since no major earthquake occurred there for at least a century, the pre-earthquake signal is supposedly purely inter-seismic with no significant curvature at the decadal scale. It shows the steady state accumulation that prevails (assuming the interface is always locked) before the earthquake and eventually leads to the seismic rupture when too much deformation has been accumulated. The stability of velocities measured there with GPS over almost 2 decades (i.e. Klotz *et al.* 2001; Brooks *et al.* 2003; Ruegg *et al.* 2009; Vigny *et al.* 2009) supports this steady-state hypothesis. In contrast, south of 38°S, the pre-earthquake signal shows clear post-Valdivia 1960 trends, with trenchward velocities still observed 40 yr after the earthquake. However, such a long time after the event, deformations also appear to be quasi-linear in time, making possible their precise estimation and removal from the post-earthquake time-series. For this work, we compile available data from various different studies (Brooks *et al.* 2003; Ruegg *et al.* 2009; Moreno *et al.* 2011; Métois *et al.* 2012) to get a pre-earthquake velocity field as dense as possible. In order to combine the different solutions we rotate them in one single consistent reference frame using common stations. In case of large discrepancies between solutions at the same station, we do not compute an average but rather keep the most recent, and supposedly most precise, velocity determination. To avoid contaminating our velocity field with unreliable velocities, we systematically reject vertical velocities determined from benchmark surveys, and only keep the vertical velocities determined at continuous sites with long records. Finally, because many new stations were installed after the earthquake, at locations where the pre-earthquake velocity was unknown, we interpolate the pre-earthquake velocity field (using cubic spline) at these new localizations (Supporting Information Fig. S1). Attributed uncertainties take into account the distances to stations with known velocities. This pre-earthquake velocity or trend is then simply subtracted from the complete time-series, so that post-earthquake trends are representative of the pure post-seismic deformation only. Then, these trends are fitted by exponential functions, which allow to fill small data-gaps and filter seasonal variations (Supporting Information Fig. S2). Several tests confirm that modelling of the seasonal variations allows to reduce the uncertainty of the long-term velocity determination, but yields the same values as the simple fit does. Only, on two specific occasions,

an additional correction is necessary: Two large aftershocks occurred [the 2010 Pichilemu earthquake (Ryder *et al.* 2012; Ruiz *et al.* 2014) and the 2012 Constitución earthquake (Ruiz *et al.* 2013)] and displaced nearby stations with an additional large co-seismic step. These steps are also estimated from the time-series themselves and removed from the post-seismic time-series. Finally, we generate average annual values of the post-seismic velocities over yearly time windows, the model being constructed to fit these. (Table of estimated velocities are provided in the Supporting Information.)

2.3 Data description

The first observation is that the post-seismic horizontal deformation extends more than 2000 km away from the trench in every direction (Fig. 1), as it was already observed, although not with such spatial continuity, in Japan after the Tohoku-Oki earthquake (Trubienko *et al.* 2014), and in SE Asia after the Sumatra-Andaman earthquake (Satirapod *et al.* 2013). Large-scale trenchward motion is observed across the continent, decreasing with distance from the trench. In the near-field, the post-seismic motions are perpendicular to the trench in front of the rupture zone of the earthquake, which differs from the coseismic displacements aligned with the plates' convergence direction. On the contrary, in the far-field, the post-seismic motions are parallel to the coseismic displacement. This difference in alignment in near-field versus far-field coseismic displacements comes from the fact that the slip on the plate interface does not keep the same direction as it deepens, suggesting that the deviatoric stresses are parallel to the relative plate direction at shallow depth but remain perpendicular to the trench at larger depth (i.e. Bai *et al.* 1992). South and North of the rupture zone, vectors are rotating, diverging from the rupture, until having a North-East orientation in the region of La Serena (31°S) and a South-East orientation in the region of Valdivia (40°S). Finally, with almost 5 yr of data after Maule earthquake, we can quantify the temporal evolution of the post-seismic deformation (Fig. 2). While near-field deformation decreases very quickly over the first 18 months following the earthquake (almost one order of magnitude), far field deformation is initially smaller but is more constant over time.

The second observation is that the ratio between the cumulative post-seismic displacement after almost 5 yr, and the respective coseismic displacement, for stations located directly in front of the rupture zone, increases with distance from the trench (Fig. 3a), from 5 per cent to 100 per cent of the coseismic jump (Fig. 3b). This ratio is not random, but rather seems to follow a distinct trend. However, this trend does not hold for stations located outside from the area in front of the rupture zone [highlighted by blue dots (Fig. 3b)]. Similar trends were observed after both the Aceh and Tohoku earthquakes (Trubienko *et al.* 2014), indicating consubstantial properties of the mantle, regardless of local particularities.

The vertical pattern is much more complicated (Fig. 4). In the near-field, close to the coast, the sign of the vertical motion depends on the latitude. First, at the latitude of Constitución (35.5°S) there is subsidence to the South and uplift to the North, which is remarkably the exact opposite of the coseismic motion (Vigny *et al.* 2011). Further North, in the area of Pichilemu (34°S) where several intraplate earthquakes occurred during the days following the Maule event (Ryder *et al.* 2012), together with consequent afterslip (Vigny *et al.* 2011; Bedford *et al.* 2013), stations are again subsiding, probably due to longer-lasting afterslip. This pattern is decreasing with time, but does not significantly reverse after 5 yr. On the contrary, in the region of Valparaíso (33°S), we observe uplift that is quickly

decreasing over the first 3 yr after the earthquake, until complete reversal (Fig. 5). During the fourth year after the earthquake, we then observe small but significant subsidence in this region ($5 \pm 2 \text{ mm yr}^{-1}$). We also clearly notice an extremely large uplift of some 3 cm yr^{-1} that starts immediately after the earthquake, along the volcanic arc, where very little coseismic vertical motion was registered (Fig. 4b, stations MAUL, ANTC). Such behaviour cannot be attributed to the reversal of the interseismic elastic accumulation, because it would then be at least one order of magnitude smaller than what is observed here (Savage 1983). This uplift pattern, located significantly far from the trench is more likely due to mantle processes. In the far-field, we do not dispose of a very dense data set and signal is smaller, but most stations show subsidence ($3 \pm 2 \text{ mm yr}^{-1}$). Similarly to (although less clearly than) the case of the 2004 M_w 9.2 Sumatra-Andaman earthquake, after which a large-scale subsidence at a rate of 1 cm yr^{-1} over 6 yr was highlighted (Satirapod *et al.* 2013). Because Maule earthquake has a significantly smaller magnitude, far-field vertical motion is expected to be of a few mm yr^{-1} only, which makes it more difficult to extract from relatively short time-series affected by strong seasonal variations. Nevertheless, 3 yr after the earthquake, subsidence is measurable in the eastern part of Argentina (Fig. 4). The vertical velocities that are presented here show high uncertainties, sometimes (not always) higher than the extracted signal. Those uncertainties reflect not only the strong seasonal signal but also the intrinsic quality of the GPS stations and the high level of noise which is known to be much stronger on the vertical component of GPS, because of atmospheric and hydrological effects that are difficult to quantify precisely. In any case, those data can hardly be interpreted confidently, and will need confirmation. However, the overall pattern is consistent with large-scale subsidence induced by the earthquake.

3 MODEL

3.1 Geometrical design of the FE model

Our FE model, schematically presented in (Fig. 6) features an overriding plate and a subducting plate (both are 70 km thick, which is a typical lithosphere thermal thickness). The subducting slab penetrates into the mantle down to 500 km depth. Geophysical evidence images the MOHO discontinuity close to 30 km at the slab contact, going down to about 40 km beneath the Andes (Krawczyk *et al.* 2006). We thus define a depth of 30 km for this discontinuity, in order to impose coherent shear moduli for the slip distribution estimation. We introduce an accretionary prism, with low elastic parameters in agreement with refraction seismic studies (Krawczyk *et al.* 2006). Our model includes a thin layer between depths of 70 and 90 km, above a 200 km thick asthenosphere and a sub-asthenospheric mantle extending down to 2800 km depth. The overriding and subducting plates and the mantle are modelled with a linear elastic behaviour. The shear and bulk moduli increase with depth according to the Preliminary Reference Earth Model (PREM) in the whole model box (Dziewonski & Anderson 1981), all elastic parameters are provided in the Supporting Information Table S3. The slab profile is based on the USGS Slab 1.0 database, taken at the latitude of the Maule earthquake. Variations of the slab geometry along the rupture zone of the earthquake are rather small (Hayes *et al.* 2012) and are neglected when building the mesh. The asthenosphere is divided in two layers, the first between 90 and 200 km depth, the second between 200 and 270 km depth. The particularity of our geometry

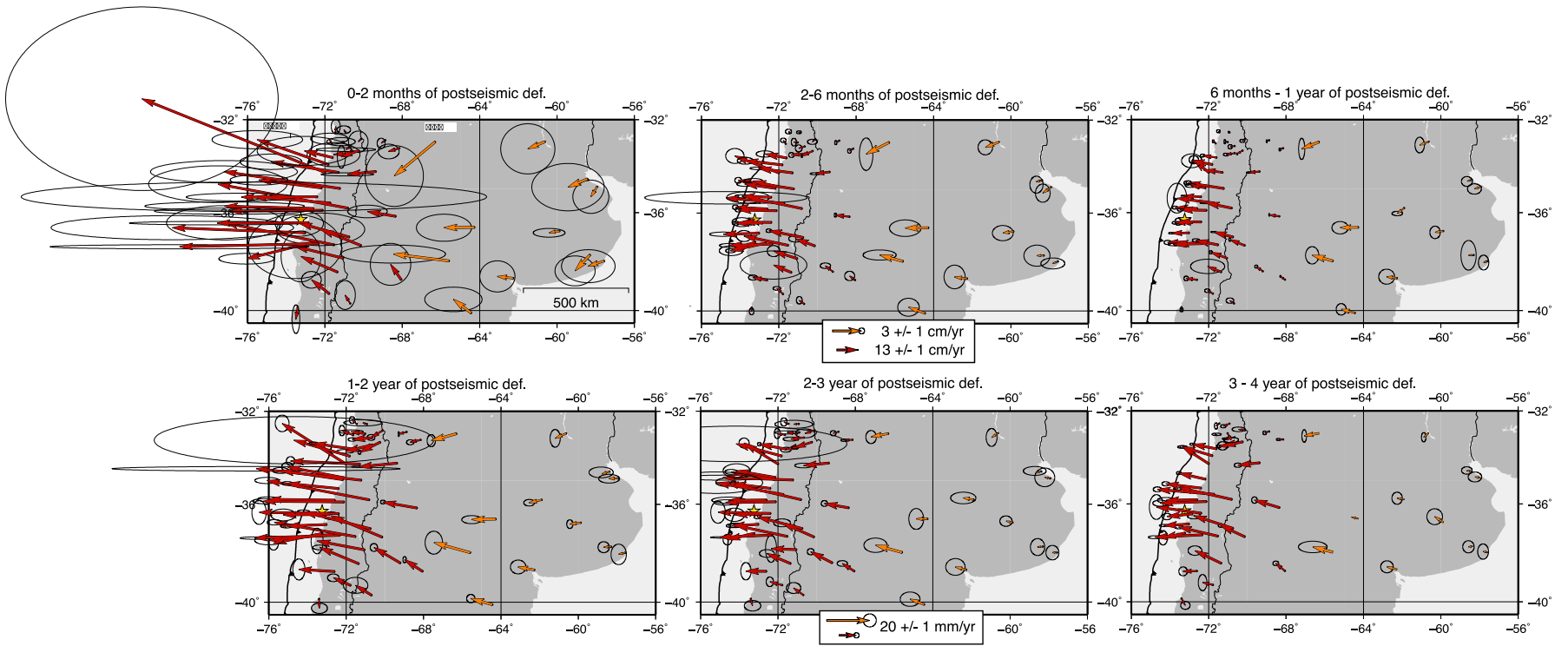


Figure 2. Temporal evolution of the mean horizontal velocity (mm yr⁻¹) during the 5 yr following the Maule earthquake—careful to the change of scale after 1 yr (fourth map).

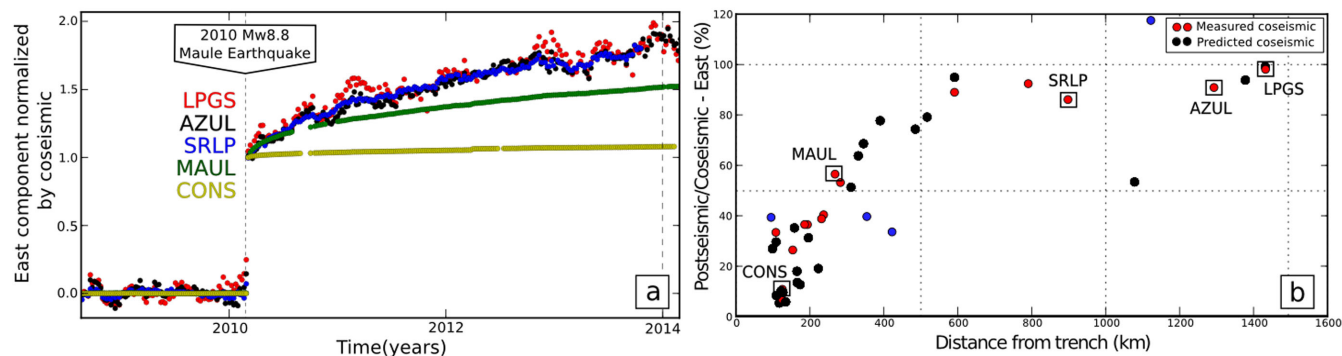


Figure 3. (a) East component of GPS time-series normalized by the coseismic displacements as function of time, for stations indicated by black square on graph (b). (b) Cumulative post-seismic displacement on the east component between 27 February 2010 and 2014 normalized by the coseismic motion (in per cent), as function of the distance from the trench. Red dots are for stations that measured the coseismic jump, the black dots are for stations installed after the earthquake (coseismic jump estimated from our coseismic slip model). Blue dots represent stations located outside the area in front of the rupture zone.

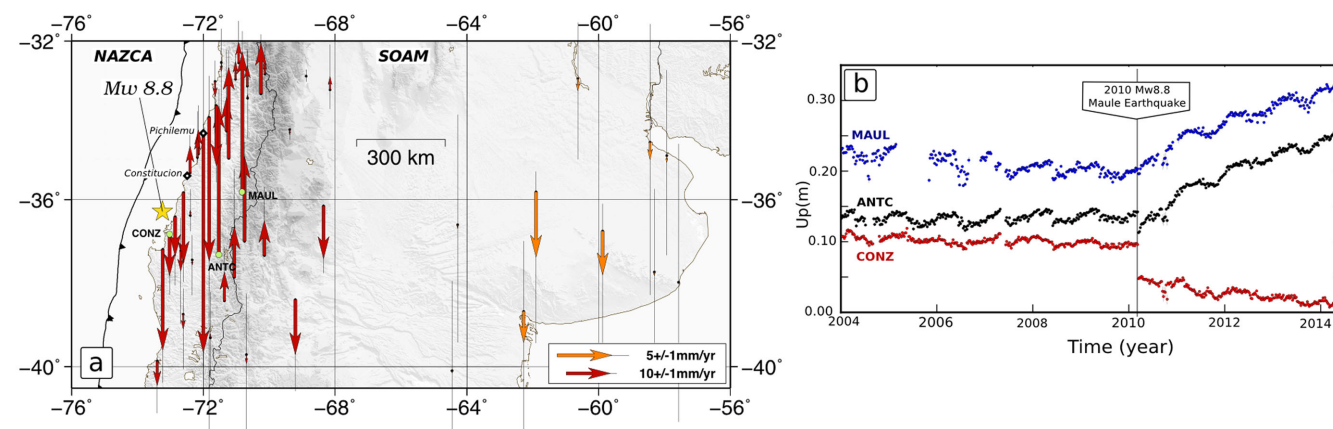


Figure 4. Vertical post-seismic velocities estimated from the GPS time-series between 2011.2 and 2012.2. (a) Mean vertical velocities (in mm yr⁻¹), ellipses depict the region of 70 per cent confidence. The yellow star depicts the epicentre of the earthquake (CSN). (b) Vertical component of GPS time-series for stations located on the map.

is the addition of two potentially low-viscosity areas: (i) a wedge above the subducting slab, extending beneath the volcanic arc, (ii) a channel extending along the subduction interface from a depth of 55 km down to 90 km, with 40 km width. We also test deeper extensions of the channel down to 135 km, with decreasing width to 25 km. The asthenosphere, the wedge and the channels have a viscoelastic behaviour, and the estimated viscosities are directly dependent on the shape of those areas (especially the width).

To model the post-seismic deformation, we use a Finite Element software Zset/Zebulon (Zset/Zebulon 8.6) in its 3-D version. The 3-D mesh (Supporting Information Fig. S3) features a spherical shell-portion from the core-mantle boundary to the Earth's surface, extending over more than 60 degrees in latitude and longitude, sufficiently large so that boundary conditions do not influence the computation results. The domain is discretized by 4-nodes 3-D tetrahedral elements (Zienkiewicz & Taylor 2000). The mesh of 46 587 nodes is refined near the fault to properly capture the strong variations of stress in this region, and the element size increases away from subduction zone by up to a factor 35, to keep an overall reasonable computational time. The mesh refinement was determined from a convergence study in which we compared results of this mesh with those of a more refined grid. A vertical force equal to $(-\rho \times g \times U_y)$ (where ρ is the density of the lithosphere, g the gravity and U_y the vertical displacement of the surface) is applied on the upper surface in order to account for gravitational forces due

to vertical uplift or subsidence (Winkler condition). To allow slip on the fault, the nodes are duplicated along the subduction interface using the split node method (Melosh & Raefsky 1983) and the earthquake is simulated by the relative displacement of the coupled nodes tangentially to the interface (Trubienko *et al.* 2013).

3.2 Methodology

3.2.1 Coseismic inversion

The coseismic stresses generated by the slip on the interface are the source of the post-seismic deformation. Many different coseismic slip models were published, based on different data sets and using different geometries but generally assuming uniform elastic parameters (e.g. Delouis *et al.* 2010; Vigny *et al.* 2011; Moreno *et al.* 2012, ...). Coseismic slip patterns inverted from models with uniform elastic parameters differ indeed significantly from those derived from more realistic models. Previous studies showed that the slip distribution is one of the major input for the post-seismic modelling (Sun & Wang 2015). So for consistency, we realize our own inversion of the coseismic slip on the nodes of the fault plane with the geometry and realistic elastic parameters used afterwards for the post-seismic modelling. To determine the coseismic slip pattern, we use all coseismic displacements measured at campaign benchmarks

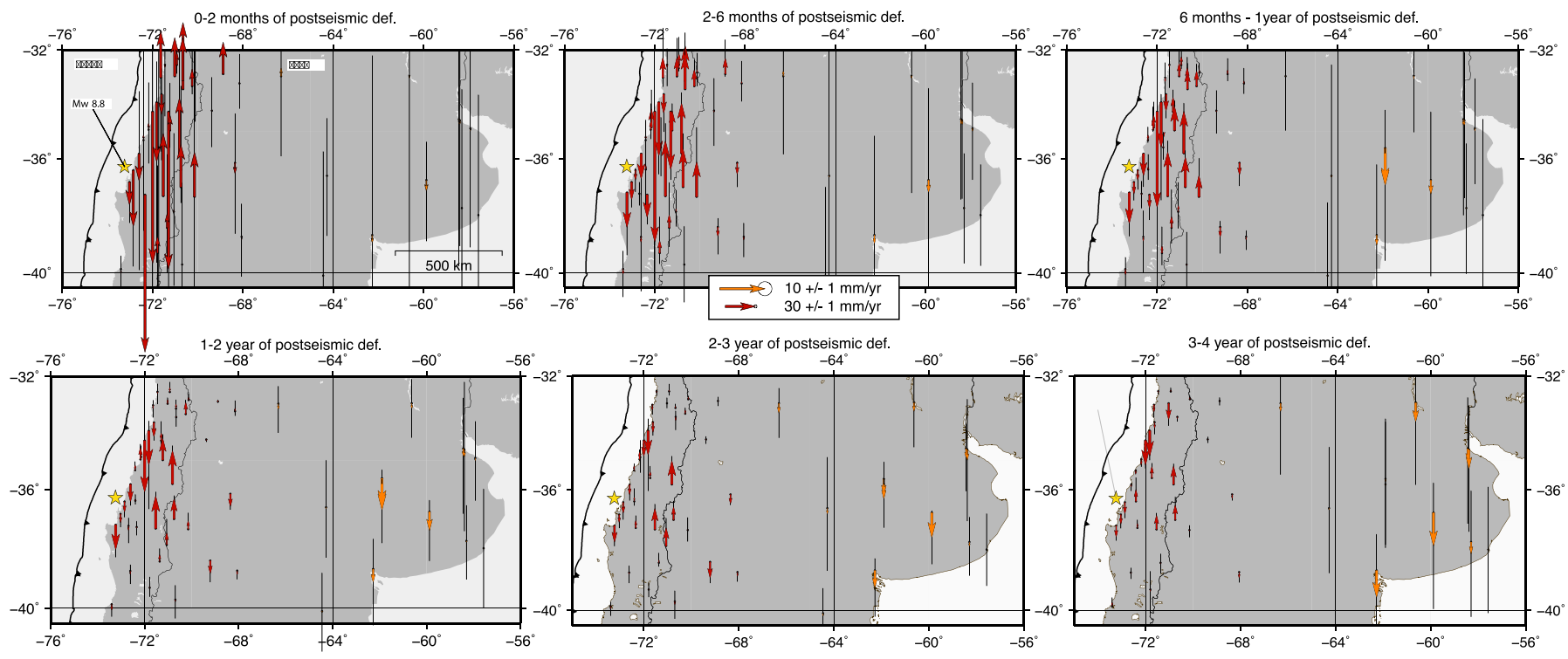


Figure 5. Temporal evolution of the mean vertical velocity (mm yr⁻¹) during the 5 yr following the Maule earthquake—same scale for every maps.

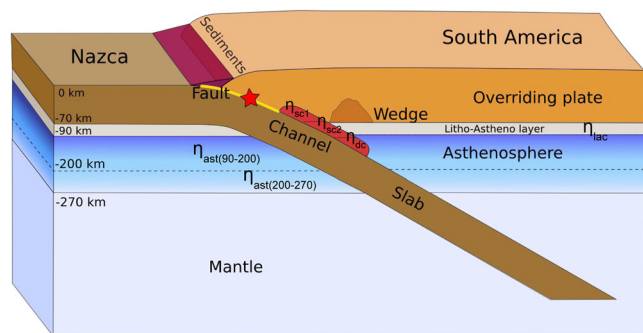


Figure 6. Geometry of the subduction interface: the elastic overriding and subducting plates are 70 km thick, the slab profile is based on the USGS Slab 1.0 database (Hayes *et al.* 2012), the asthenosphere is 200 km thick and is viscoelastic. The low-viscosity channel above the slab extends down to 135 km. The fault plane is represented in yellow, and the red star depicts the location of the typical epicentre of megathrust earthquakes.

and at permanent stations published by Vigny *et al.* (2011). We also add a few GPS sites published by Delouis *et al.* (2010), Tong *et al.* (2010), Moreno *et al.* (2012) and Lin *et al.* (2013). Because surveys are conducted several days (or weeks) after the earthquake, many of these measurements are contaminated with early post-seismic deformation. We homogenize the data set by integrating the first 12 days of displacements to the purely coseismic motions, at all sites.

Along-dip and along-strike Green functions are calculated for each node of the grid. The coseismic slip distribution is determined using a least-square technique. We limit the zone of possible slip to 55 km depth, and latitudes between 32 and 39°S, corresponding to the area of aftershocks (Lange *et al.* 2012). We allow the rake angle to vary between $\pm 56^\circ$. The relative weight of near-field versus mid-field and far-field data has been adjusted so that the final fit (in percentage) is similar for the three types of data. Typically, we impose a coefficient 1/20 on far-field data in order to take into account the relative error over amplitudes drastically different between near/mid field and far field. A slight damping is introduced through a term in the penalty function proportional to the square of the amplitude of the slip on each node (one peak slip of 33 m on one node has the same cost as a misfit of 0.7 m on one data point).

3.2.2 The steepest slope method

We impose a Burgers rheology (which will be discussed later in this paper) to all viscous areas. The response of a Burgers body to a sudden increase of stress is characterized by an instantaneous elastic strain (proportional to $1/\mu_M$), a long-term viscous strain rate (proportional to $1/\eta_M$) and transient creep which decreases as a function of time [Kelvin-Voigt block where $1/\mu_K$ governs the total amplitude of the transient phase and where η_K is the short-term viscosity (see Supporting Information Fig. S4B)]. Each area is characterized by its own steady-state Maxwell viscosity η_M . We keep the ratio between the two viscous parameters constant as well as the ratio between the modulus of the Kelvin-Voigt element and the elastic modulus (μ_K/μ_M), in order to limit the number of free parameters to estimate by inversion. We discretize the channel in three sections in order to try to account for variations of viscosities depending on depth. The relevance of these areas in the final model will be discussed in this paper. Therefore, we initially have a set of eight free parameters: the long-term viscosity of six areas, and the two ratios μ_K/μ_M and η_M/η_K , the latter allowing to determine the

Kelvin-Voigt viscosities of each viscous area. We search for the set of those parameters which allow to achieve the best fit to the post-seismic velocities determined over the first 2 yr after the earthquake, adding a weight three times larger on the second year. Having done the modelling before the full 5 yr data set became available, we use these first 2 yr only, which also appear to have the maximum signal over noise ratio, especially on the vertical. We use for that a steepest slope method, which is based on iterative computations of the partial derivatives of the produced deformation with respect to the free parameters of the system. Note that this is a nonlinear problem since the total response at the surface is not equal to the sum of the responses due to relaxation in each viscous area. The partial derivative computation consists on the difference between post-seismic velocities predicted by the reference model and velocities predicted by a model for which we impose a slight variation (20 per cent) of one of the free parameters, calculated for each unknown. Initial parameters values for the inversion are chosen from a previous study of the post-seismic deformation following the Tohoku earthquake; one partial derivative is then calculated per unknown. This method leads to adjustments of initial values and misfit reduction (Trubienko 2013). Since the known drawback of this method is that it can converge to local rather than absolute minimum, we reiterated our computations beginning with different initial viscosity values in the range 10^{17} – 10^{19} Pa s, to confirm that it led to the same minimum. Finally, we invert simultaneously for the multiplicative factors of viscosity parameters in the different zones and the afterslip on the fault plane, which unknowns are the Green functions previously calculated, using a standard least-squares algorithm, with a weighted L2 norm cost function. We decide to invert simultaneously for both the aseismic slip on the fault plane and the rheology parameters, in order to account for the amount of viscoelastic relaxation induced by the afterslip. Similarly to the coseismic slip distribution inversion, we do not authorize slip beyond a depth of 55 km. Below this depth lies the channel, where relaxation will occur rather than slip. The steepest slope method is cost effective compared to a Monte Carlo approach which needs to explore systematically and blindly the entire parameter space, which is not appropriate for a heavy 3-D FEM.

4 RESULTS

We present in this section the main results of this study, with first the coseismic slip distribution that was inverted. After showing that an afterslip-only model cannot reproduce the observed pattern, we focus on the effect of the relaxation in each viscous areas, with simple forward models. Then we test a model of viscoelastic relaxation only for which the viscosities for each region providing the best fit to post-seismic data are inverted. We finally show why this model of viscoelastic relaxation alone also fails to reproduce the surface deformation and discuss the relative importance of both mechanisms.

4.1 Coseismic slip distribution

Our inverted coseismic slip distribution is represented on Fig. 1. Since we have elastic heterogeneous parameters, we compute two values of the seismic moment, the first one using the elastic parameters distribution from the oceanic plate, the second one using the elastic parameters distribution from the continental plate. We obtain values of $M_0 = 4.44 \times 10^{22}$ N m, respectively $M_0 = 1.9 \times 10^{22}$ N m, corresponding to equivalent magnitudes of 9.0, respectively

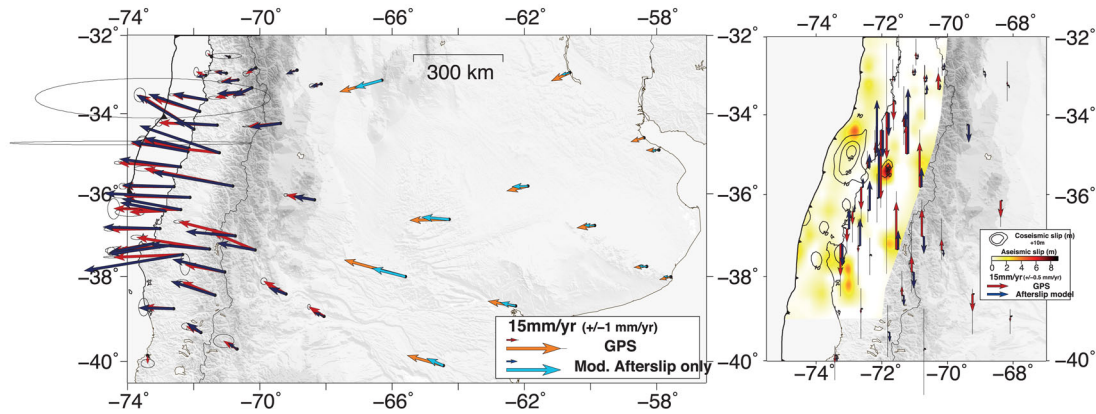


Figure 7. Observed versus predicted velocities (mm yr^{-1}) between 2011.2 and 2012.2, in the case of a pure afterslip model (without VER), horizontal (left) and vertical (right). The slip distribution of afterslip, corresponding to the same period, is represented in colour scale (in m). Black contours (+10 m) represent the coseismic slip distribution inverted in this study.

8.78. The seismic moment for our model corresponds to a value in between those two and is coherent with the seismological estimate of 2.39×10^{22} N m (Hayes *et al.* 2012). Our coseismic slip distribution presents a maximum slip of the order of 30 m in the hypocentral area, which is larger than previously published values (close to 20 m, i.e. Vigny *et al.* 2011; Moreno *et al.* 2012, ...), mainly coming from the fact that we do not use a smoothing function in our inversion. The damping function we use aims at penalizing high slip on localized node, but we do not impose any cut-off and this explains the larger local maximum slip compared to previous studies. Otherwise, our slip model is consistent with previous models, with the maximum slip area in the north of the rupture area, near 35°S , and a second zone of large slip south of the epicentre, near 37°S which reaches the surface, consistent with the large tsunami induced in the area (Vargas *et al.* 2011). Modelled displacements fit well the observations with a mean horizontal residual of 12 cm (2.5 per cent of the signal) and mean vertical residual of less than 3 cm. Maximum residuals are all found on the Arauco Peninsula, especially on campaign markers (Supporting Information Fig. S5), which could be explained by either additional displacements on local faults (Melnick *et al.* 2012) or local afterslip. Obviously, and because it is largely under-constrained, the coseismic slip distribution is not unique. The obtained source model depends on parameters like chosen geometry, elastic parameters, variable relative weight of near-field versus far-field data, damping or smoothing, imposed maximum depth of slip, etc... Finally, we propose here an average model with a slip distribution not as deep as in Lorito *et al.* (2011), Lin *et al.* (2013) but deeper than in Vigny *et al.* (2011), Yue *et al.* (2014), which appears very similar to the one proposed by Moreno *et al.* (2012), with one maximum slip patch in the North of the epicentre and significantly smaller patches in the South.

4.2 Inversion of an afterslip-only model

We first test a simple model of pure elastic afterslip, i.e. inverted without viscous parameters. In this model, slip is allowed down to 90 km. Fig. 7 shows the afterslip distribution over the second year after the earthquake and the associated fit to data. The slip amplitude is very strong (maximum of 10 m slip). This distribution is quite different from previous afterslip-only models (Bedford *et al.* 2013; Lin *et al.* 2013) that find slip mainly at intermediate depth, beneath the coast. However, this distribution, somewhat anticorrelated with the coseismic distribution, makes sense. In particular, we find a large

patch of afterslip off Navidad and Pichilemu (34°S), where repeated seismic swarms occurred over the 2 yr following Maule earthquake (Fig. 7). We also find an isolated patch at the latitude of Constitución (35°S), immediately below the epicentral area of a large aftershock which occurred afterwards, the Constitución earthquake of 2012 (Ruiz *et al.* 2013).

This pure afterslip model fits well the near- and mid-field horizontal velocities but misfits the far-field velocities by almost a factor 2. The vertical pattern cannot be reproduced by this model. Fitting the near-field vertical velocities would only be possible at the cost of the horizontal fit. Moreover, even deep slip on the fault plane cannot produce the quick uplift over the Cordillera and predicts zero vertical motion further than 300 km from the trench.

Consequently, an afterslip-only model is not satisfying. Fig. 7 clearly illustrates the need for another process inducing subsidence in the near-field and enhancing the far-field velocities. Thus we explore in the next sections more complex models involving viscoelastic relaxation.

4.3 Impact of relaxation in low-viscosity areas on surface deformation—synthetic tests

The necessity of several different low-viscosity zones comes from the fact that relaxation in each of them does not produce surface deformation with the same spatial pattern. In this section, we describe the impact of relaxation in each zone separately. To do so, we compute synthetic forward models in which all layers are purely elastic except the tested one. The viscosity of the tested zone is arbitrarily fixed to $\eta_M = 3 \times 10^{18}$ Pa s for all cases. Therefore, it should not be compared to the results of inversions and the complete best fit model presented in the end. For more clarity, in these tests, we discretize the channel in two sections only, a shallow and a deep one, to precisely highlight their effect on surface deformation.

Relaxation in the asthenosphere induces deformation over more than 2000 km away from the trench in all directions. The oceanic and continental sides of the asthenosphere have the same rheological characteristics and viscosities. We show here the effect of relaxation in the upper layer of the asthenosphere. The pattern induced by relaxation in the lower layer is the same though with a weaker amplitude due to its low thickness but also its depth and localization compared to the coseismic area, which imply weaker stresses. Relaxation in the asthenosphere produces two main

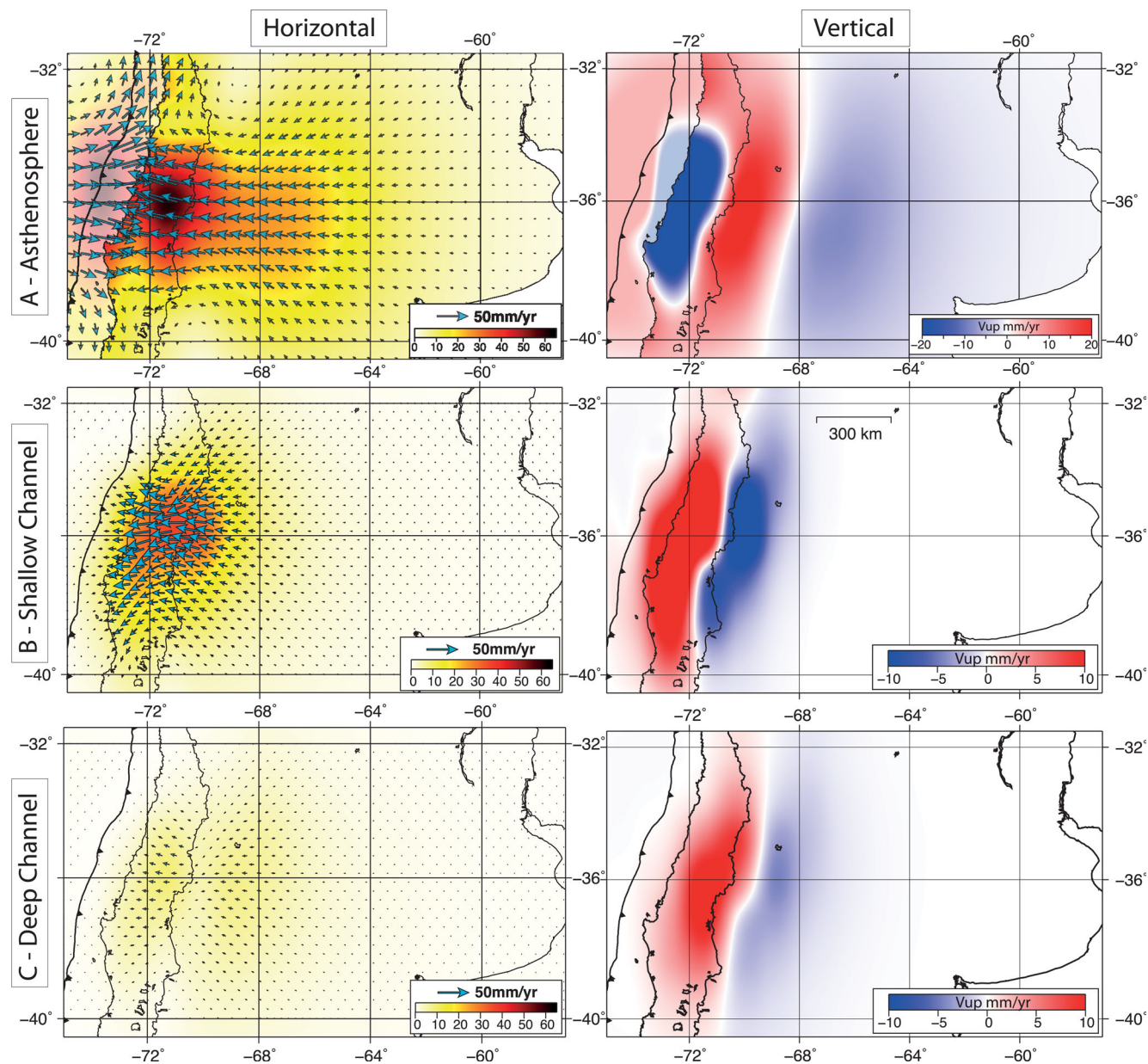


Figure 8. Effect on horizontal (left: in mm yr^{-1} , colour scale represents amplitude) and vertical (right: V_{up} in mm yr^{-1}) surface velocities of relaxation in different viscous areas: (a) due to relaxation in the upper layer of the asthenosphere; (b) due to relaxation in the shallow channel only; (c) due to relaxation in the deep extension of the deep channel (down to 135 km).

deformation spots, with velocities of 60 mm yr^{-1} over the first year after the earthquake. The first spot is localized at the level of the trench and is controlled by the oceanic side of asthenosphere featuring landward deformation, along the first 70 km from the trench. The second spot of major slip is localized inland, still on the western side of the Cordillera, featuring trenchward deformation (Fig. 8a-left). South, respectively North, of the rupture zone, the convergence between the landward, respectively trenchward, orientation generated by the relaxation of the oceanic, respectively continental asthenosphere, induces a ‘return flow’: diverging motion from the rupture zone up to a complete rotation inland towards southeast in the south, and northeast in the north (Figs 8a and Supporting Information Fig. S7). Concerning vertical displacements, relaxation in the asthenosphere induces subsidence in the first 300 km from the trench, directly in front of the rupture zone, uplift of a 200 km wide

belt in all directions, particularly marked on the East side of the Andes, and finally, general subsidence in the far field (Fig. 8a-right). Thus, relaxation in the asthenosphere is required to fit the observed far-field deformation. However, the amplitude of the deformation it generates in the mid-field is not sufficient compared to the observations and it predicts a landward orientation in the near-field which is not consistent with the observed pattern (Fig. 8a-left). We thus test the presence of a shallow channel, meant to increase relaxation in a given and limited area.

Relaxation in a shallow channel indeed induces deformation mainly localized in the mid-field (Fig. 8b) but with very limited effect in the far-field. Therefore, relaxation in a channel alone would also not fit the data. Both the asthenosphere and the channel are necessary to fit the far-field deformation pattern on one hand, and to boost the horizontal mid-field deformation on the other hand.

Table 1. Table of the steady-state viscosities of the pure viscoelastic relaxation model ($\mu_K = 2.6 \times \mu_M$) and of our preferred combined model ($\mu_K = 3.9 \times \mu_M$), in both cases, $\eta_M/\eta_K = 6.5$. Initials of areas refer to the sketch, Fig. 6.

Area		VER only η_M (Pa s)	Combined model $\eta_M \times 10^{\sigma_M}$ (Pa s)
SC1	Shallow channel 1 (55–70 km)	1.3×10^{18}	$6.7 \times 10^{18} \times 10^{\pm 0.2}$
SC2	Shallow channel 2 (70–105 km)	3.4×10^{17}	$3.35 \times 10^{17} \times 10^{\pm 0.2}$
DC	Deep channel (105–135 km)	5.7×10^{17}	$7.15 \times 10^{17} \times 10^{\pm 0.5}$
LAC	Lithosphere–asthenosphere continental layer (70–90 km)	2×10^{18}	$5.6 \times 10^{18} \times 10^{\pm 0.5}$
Asthenosphere	90–200 km	3×10^{18}	$4.75 \times 10^{18} \times 10^{\pm 0.03}$
Asthenosphere	200–270 km	8.4×10^{18}	$1.9 \times 10^{19} \times 10^{\pm 0.6}$
Slab		Elastic	Elastic
Overriding plate		Elastic	Elastic
LAO	Lithosphere–asthenosphere oceanic layer (70–90 km)	Elastic	Elastic
Mantle		Elastic	Elastic

This model, with relaxation in a low-viscosity channel no deeper than 70 km, also predicts a line of zero-vertical motion on the Western side of the Cordillera, before the Chile–Argentina border, with uplift to the west of this line and subsidence to the east (Fig. 8b–right). However, one of the remarkable features of the post-seismic deformation pattern is the uplift of 3 cm yr^{-1} in the mid-field.

Relaxation in a deep channel, extending down to 135 km depth, has little effect on horizontal deformation (Fig. 8c) but shifts the zero-vertical motion line eastward, and broadens the uplift zone, which then better reproduce the observed pattern over the volcanic arc.

Relaxation in a wedge, at depth between 50 and 70 km above the subducting plate, potentially extending beneath the volcanic arc, induces a comparable but weaker effect, both in horizontal and vertical, to that of the shallow channel (Supporting Information Fig. S6). But the presence of the low-viscosity wedge does not improve the fit to the data, in particular in vertical, because it cannot produce the quick uplift over the volcanic arc. Therefore, we consider that its existence is not supported by the data and exclude it from all the following models.

4.4 Inversion of rheological parameters for a model of pure viscoelastic relaxation

In this subsection, we report trials to reproduce the post-seismic pattern using a model of pure viscoelastic relaxation, without afterslip on the subduction interface. Note that the effect of relaxation in those different areas is not linear, i.e. the total response is not the sum of the responses due to relaxation in each of them, (other regions being assigned purely elastic behaviour). Moreover, the vis-

cous layer at depth 70–90 km below the ocean appears to have no impact on the predicted post-seismic deformation on land. So elastic properties are assigned to this area. Therefore, we test in this section a rheological model in which the two layers of the asthenosphere, the continental lithosphere–asthenosphere layer (70–90 km) and the channel discretized in three sections, are viscous with Burgers rheologies and we invert their viscosities. Finally, eight parameters are left free: the long-term viscosity of the six areas, and the two ratios μ_K/μ_M and η_M/η_K .

In that case, testing only relaxation (not taking afterslip into account), the preferred model features an asthenosphere with a steady-state Maxwell viscosity of $3 \times 10^{18} \text{ Pa s}$ to account for the large-scale post-seismic deformation, and a low-viscosity channel extending down to 135 km depth, for which the viscosity of the shallow part, between 1.3×10^{18} and $3 \times 10^{17} \text{ Pa s}$, is constrained by the horizontal data in the mid-field and the viscosity of the deep part, equal to $6 \times 10^{17} \text{ Pa s}$, is constrained by the vertical mid-field pattern. The ratio between the viscous parameters is set to $\eta_M/\eta_K = 6.5$. The relaxed modulus of the Kelvin–Voigt part is 2.6 times stiffer than the elastic modulus ($\mu_K = 2.6 \times \mu_M$). Due to the large value found for μ_K , the Kelvin–Voigt element mainly affects the first months of the post-seismic evolution. This small and early Burgers deformation will deserve to be better constrained using a data set description involving smaller time-steps during the first year. All parameters are summarized on Table 1.

This model fits well both horizontal and vertical post-seismic patterns in the mid- and far-field directly in front of the rupture zone (Fig. 9) over the first 2 yr after the earthquake. It also predicts well the North–East trending motion that is visible in the region of La Serena, north of 32°S (Supporting Information Fig. S8), a pattern entirely due to the relaxation in the asthenosphere and its ‘return flow’

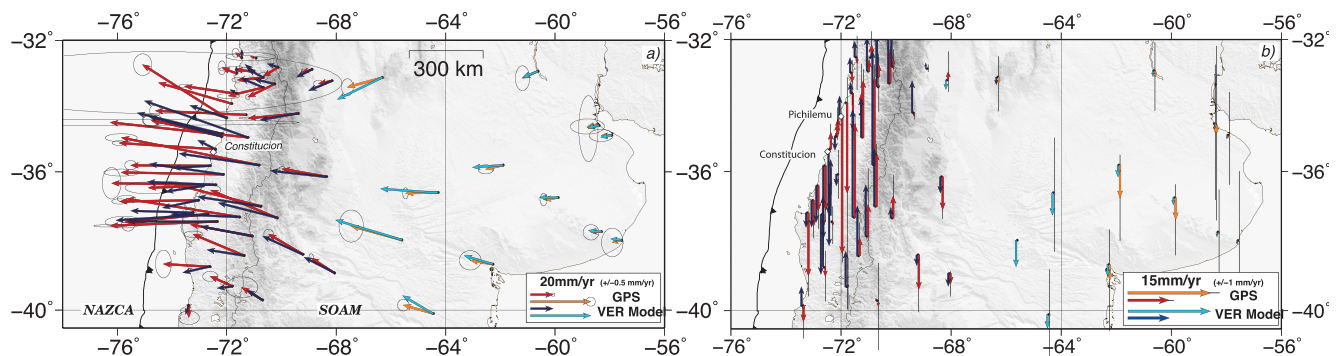


Figure 9. Observed versus predicted mean velocities (mm yr^{-1}) between 2011.2 and 2012.2, in the case of a pure viscoelastic relaxation model (viscosities indicated on Table 1): (a) horizontal velocities, (b) vertical velocities.

(Fig. 8a—Supporting Information Fig. S7). Nevertheless it fails to explain the very large amount of displacement measured in the near-field (Fig. 9a), including the region of Pichilemu. Additionally, relaxation only cannot explain the change of sign of the vertical velocities along the coast (Fig. 9b). The comparison of post-seismic data acquired both on the oceanic and continental plates suggested no evident variation of viscosity across the slab (Trubienko *et al.* 2014). However, we test the effect on surface deformation of attributing a very high viscosity to the oceanic asthenosphere, 1×10^{20} Pa s, following Hu *et al.* (2004). This does not improve the model in the near-field, but on the contrary deteriorates the fit to the data in the region of La Serena (32°S, North of the Maule rupture zone). Moreover, it has no effect on the mid- and far-field (see in the Supporting Information Fig. S9 and more details). Therefore, we attribute a unique viscosity to the asthenosphere in the following models.

4.5 Impact of viscoelastic relaxation versus afterslip

Numerous studies try to reproduce post-seismic deformation with either afterslip or viscoelastic relaxation independently (e.g. Bedford *et al.* 2013; Han *et al.* 2014). Others consider both mechanisms but first correct data from the viscoelastic relaxation effect, and then invert in a second step for the amount of shallow afterslip necessary to reproduce the near-field data (Suito & Freymueller 2009). Our main point here is to invert for both phenomena simultaneously. Moreover, aseismic slip on the fault plane also generates additional viscoelastic relaxation in the viscous layers of the Earth, which will show mostly in the mid- and far-field. It is then necessary to consider not only the viscoelastic relaxation response to the

coseismic slip and the elastic aseismic slip on the fault plane but also the viscoelastic relaxation response to this shallow afterslip. In the case of our inverted slip models (coseismic and afterslip), the relaxation induced by afterslip on the fault plane represents up to 10 per cent of the relaxation induced by the coseismic slip. This has sizable effect on horizontal deformation, even in the far-field (Fig. 11: GPS time-series of station LPGS). Studies accounting simultaneously for those three components are generally associated to simple two-layers geometry, featuring an elastic lithosphere, without slab, overlying a homogeneous Maxwell asthenosphere (Diao *et al.* 2014; Yamagiwa *et al.* 2015). However, we believe that effects of the viscoelastic relaxation (both of coseismic slip and afterslip) are biased because of the simplicity of such a geometry.

The simultaneous inversion of afterslip on the fault plane and the rheological parameters lead to the preferred model presented in (Fig. 10), with the rheological parameters reported in table (Table 1) and the afterslip distribution over the second year after the earthquake presented in (Fig. 10b). The slip distribution of afterslip over the first year and the fit to data is provided on Supporting Information Fig. S10. The correlations between the effects of inverted viscosities are relatively small (see Correlation matrix Table S3 and Fig. S12 in Supporting Information), supporting the fact that there is little trade-off between the viscosities of these areas, and that they can be determined independently, even if uncertainties increase with depth. Nevertheless, the lower asthenospheric layer (between 200 and 270 km) can hardly be constrained using the surface deformation, due to its depth, as evidenced by its high uncertainty ($\sigma_M = 0.6$). The viscosity is thus fixed to a rather high value of 1.9×10^{19} Pa s. We also estimate an error of 2.5 per cent over the

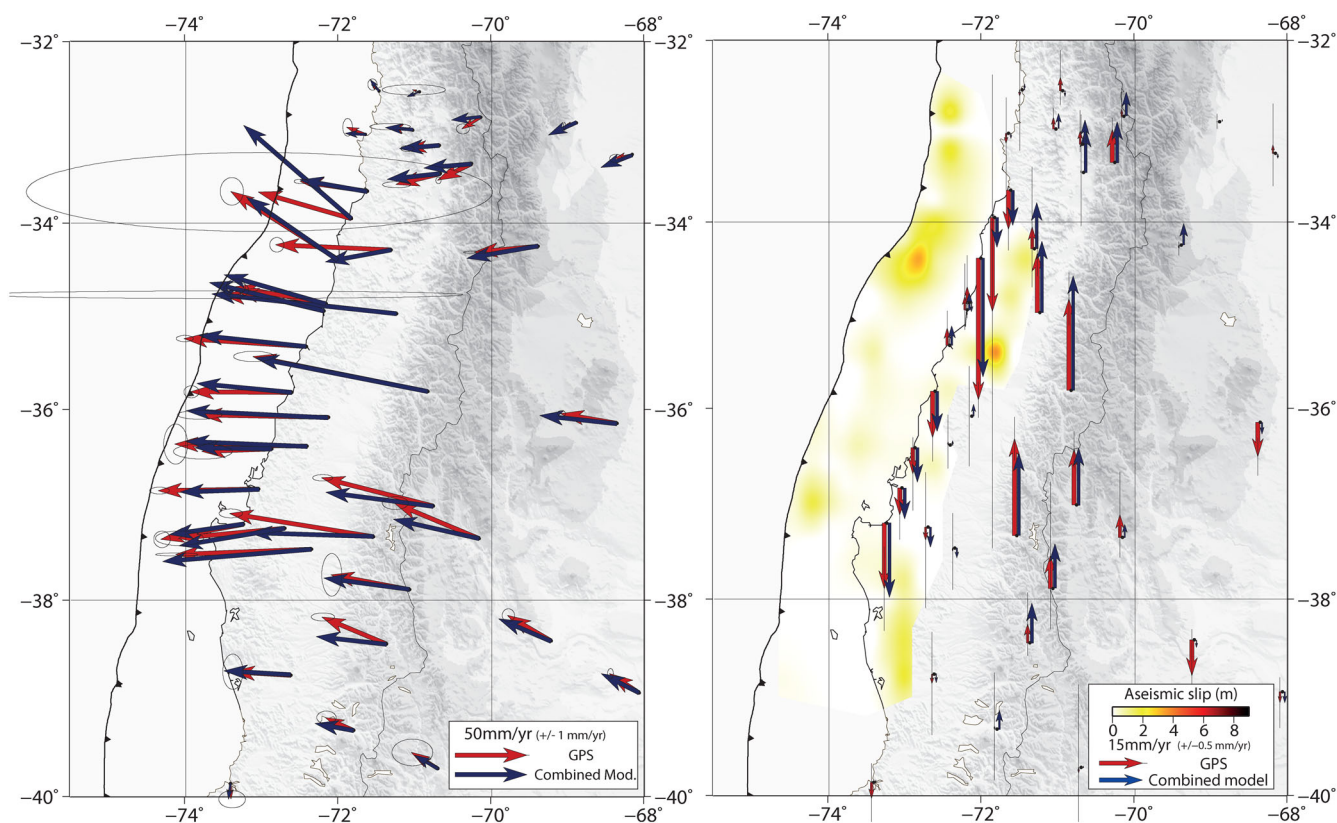


Figure 10. Observed versus predicted mean velocities (mm yr^{-1}) between 2011.2 and 2012.2, in the case of a combined model of viscoelastic relaxation and afterslip—left: horizontal velocities; right: vertical velocities. The slip distribution of afterslip, corresponding to the same period, is represented in colour scale (in m).

total amplitude of slip (see the Supporting Information for more details). The relaxed modulus of the Kelvin–Voigt part is now 3.9 times stiffer than the elastic modulus ($\mu_K = 3.9 \times \mu_M$). The major difference with the viscosities obtained from the model with relaxation only (without afterslip, Section 4.3) is the upper channel viscosity which is now multiplied by a factor of 5 and reaches 6.7×10^{18} Pa s. The asthenosphere is also slightly more viscous with a viscosity value of 4.7×10^{18} Pa s, with very small uncertainties ($\sigma_M = 0.03$).

Our model puts afterslip mostly updip the coseismic rupture zone, since a large part of the possible downdip slip is taken into account by the relaxation in the channel. Since the afterslip-only model tested in Section 4.2 does not produce the correct amount of mid-field uplift, even when deep afterslip is authorized, we conclude that relaxation in a low-viscosity channel along the subduction interface is a better description of the deformation occurring there. Furthermore, note that the relaxation in the channel implies a deformation simply proportional to the stress induced by the Maule earthquake, while the geometric pattern of the afterslip implies a much larger number of free parameters.

The time-dependence of afterslip remains a tricky point since in this study, slip is inverted on annual time windows. In order to continuously introduce the slip and compare our model to GPS time-series, we roughly estimate a time function, according to which more than 50 per cent of the slip is released over the 50 first days after the earthquake, more gradually afterwards. But the time function appears to vary quite significantly with space. Therefore, it should be inverted together with the slip over shorter time windows. This will be the topic of future study. The general pattern of slip on the interface inverted in this section is very similar to the afterslip-only model, with a patch of strong shallow slip off Navidad and Pichilemu ($\sim 34.5^\circ$ S) and a stronger one below the epicentral area of the Constitución earthquake. However, the slip amplitude is significantly weaker (less than 3 m over the second year versus a maximum of 10 m in the afterslip-only model), there again since a large part of the deformation is taken into account by the relaxation in the channel.

5 DISCUSSION

We inferred from the synthetic tests conducted above that neither viscoelastic relaxation nor afterslip alone can fully explain the observed post-seismic deformation at all scales. Thus, the complete model uses a combination of both, not forgetting the added relaxation induced by afterslip. In the following section, we discuss the rheologies of all viscous areas of our preferred combined model. We also discuss potential heterogeneities in the asthenosphere linked to the presence of a cratonic tectosphere. We finally open new perspectives on the contribution of post-seismic deformation to the seismic cycle that shows in regional (Argentina) small deviations of the observed deformation with respect to the homogeneous model.

5.1 Temporal evolution of the model and discussion concerning Burgers rheologies

The viscosity of the asthenosphere inverted in this study appears to be higher than predicted by previous finite element models that do not feature any channel but only a mantle and an oceanic mantle wedge (Hu & Wang 2012; Sun & Wang 2015). The channel allows to account for a large part of the deformation in mid-field which explains our higher asthenosphere's viscosity. On the contrary, models using a more simple two-layer geometry yield Maxwell rheologies with even higher viscosities of the order of 10^{19} Pa s (Yamagiwa *et al.* 2015). Note that the amplitude of the short-term Kelvin–Voigt deformation used here is rather modest ($\mu_K = 3.9 \times \mu_M$). However, without this transient creep, a larger slip would be needed in order to fit the post-seismic displacements during the first year in the mid-field, inducing too large near-field displacements (Fig. 11–station MAUL).

The model proposed in this study is built using the first 2 yr of data, but its prediction over a longer time period can be tested and compared with the GPS data. Our model predicts well horizontal deformation in mid- and far-field beyond the 2 yr over which it has been adjusted, with a slight deviation in Central Argentina that will be discussed further. 5 yr after the earthquake, the discrepancy

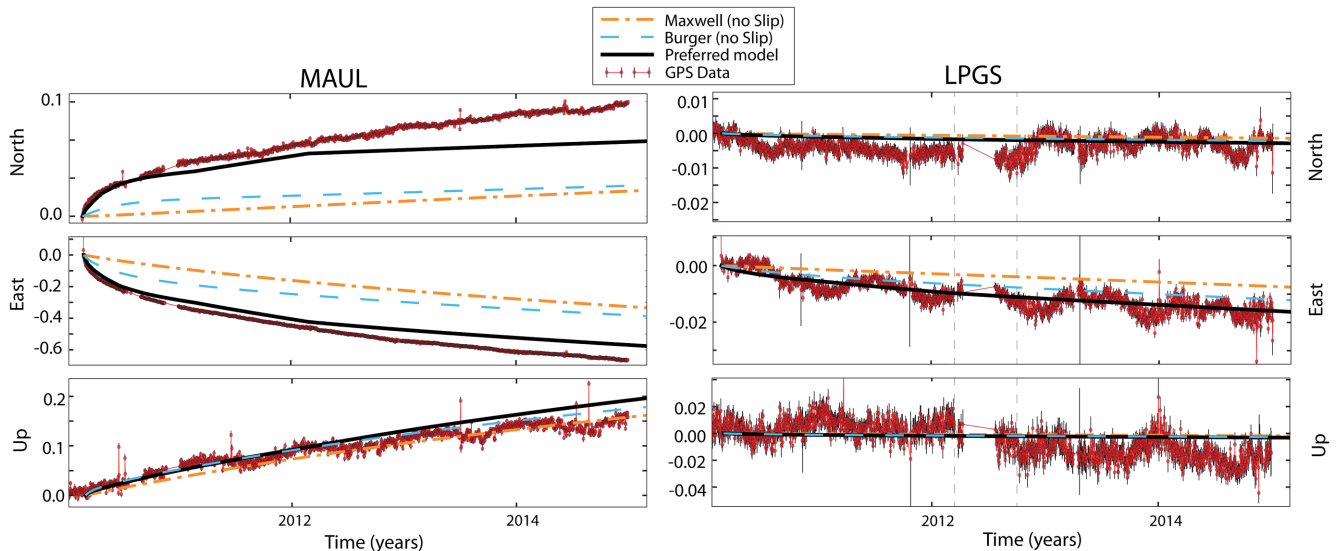


Figure 11. Time-series of GPS data (red) versus three models—orange: model of viscoelastic relaxation only with Maxwell rheologies (viscosities equal to the steady state viscosity of our preferred Burgers model); blue: viscoelastic relaxation only with Burgers rheologies; black: preferred combined model of viscoelastic relaxation with Burgers rheologies and afterslip (aseismic elastic slip + viscous relaxation induced), for a near-field station MAUL (left), and a far-field station LPGS (right). Grey dashed lines mark known dates of material changes.

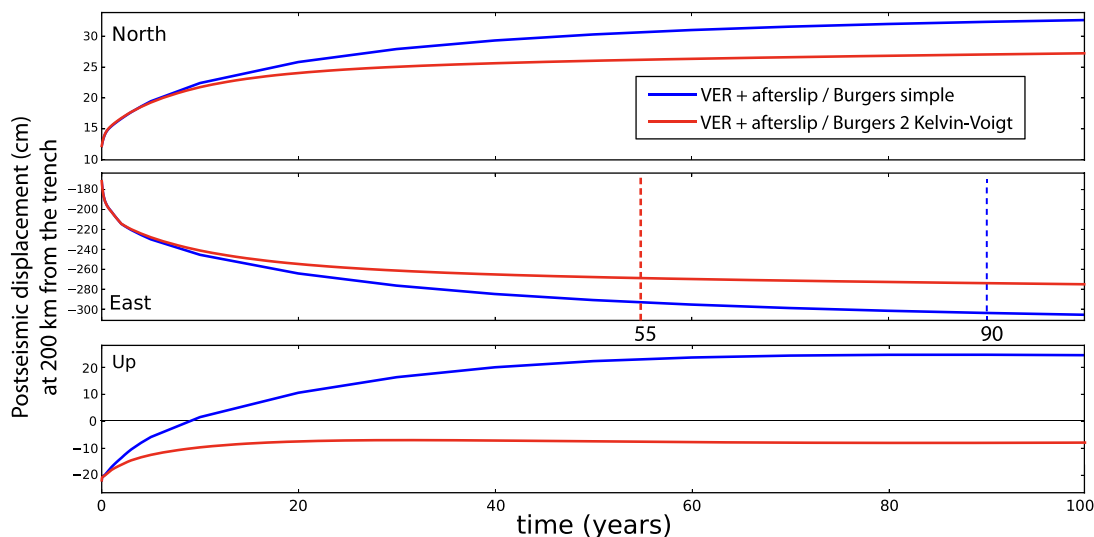


Figure 12. Post-seismic surface displacements at a point located 200 km away from the trench for two models—blue: preferred combined model $\mu_K = 3.9 \times \mu_M$, and viscosity parameters defined in Table 1; red: combined model for the complex rheology defined by a steady-state viscosity $\eta_M = 3 \times 10^{19}$ Pa s, $\eta_{K1} = 4.8 \times 10^{18}$ Pa s (asth.), $\mu_{K1} = 3.9 \times \mu_M$ (first Kelvin–Voigt element) and $\eta_{K2} = 7.4 \times 10^{17}$ Pa s (asth.), $\mu_{K2} = \mu_M/5$ (second Kelvin–Voigt element) (sketches of the two rheologies are given in Supporting Information Fig. S4). The dashed lines on east component mark the approximate date at which less than 2 mm yr^{-1} is predicted, the colours are respective to the curves.

between model and observations is less than 20 per cent of the signal on the east component. For example, at the station RGAO (mid-field), which has a horizontal velocity of 22 mm yr^{-1} after 3 yr, the discrepancy with the model is only 3 mm yr^{-1} . At the station VBCA (far-field), which has a horizontal velocity of 6 mm yr^{-1} , the discrepancy is of 1 mm yr^{-1} . Still, our model does not predict enough deformation in near field after 2 yr. This is an indication that afterslip on the fault plane may still occur beyond the second year, meaning a third year of afterslip, and its associated relaxation, should be inverted and added to the model. Our model also predicts a decrease of the far-field subsidence that is not yet observed (Fig. S11). Obviously, the cumulated subsidence itself is small (no more than several cm over 5 yr), so that its variation with time is rather undecipherable. Longer time-series are needed to clarify this point.

A very important comment: values of several 10^{18} Pa s can hardly account for a steady-state, long-term viscosity. They are too small. They yield horizontal deformation larger than 2 mm yr^{-1} up to 90 yr after the earthquake (Fig. 12). If this were true, present-day post-seismic deformation following the Valdivia earthquake would be 10 times larger than observed presently, considering that the moment of the Valdivia earthquake is almost ten times higher than Maule’s. The viscosities inferred from this study may rather correspond to transient viscosities over maybe a decade, before revealing ‘real’ steady-state viscosities of the order of 10^{19} Pa s. Such values would then be in agreement with studies based on the Valdivia earthquake data (Khazaradze *et al.* 2002; Hu *et al.* 2004). More complex rheologies, with several Kelvin–Voigt elements could represent such a behaviour (See Fig. S4–C in Suppl.). A model with a steady-state viscosity of 3×10^{19} Pa s, two Kelvin–Voigt elements, one characterized by $\mu_K = \mu_M/5$, predicts, more reasonably, horizontal velocities of less than 2 mm yr^{-1} 55 yr after the earthquake, while the first 5 yr remains similar to the current model presented here at 200 km from the trench (Fig. 12). At this distance, discrepancies between models with a simple Burger and models with a second Kelvin–Voigt element reach less than 2 cm of cumulated displacement after 5 yr (presently), of 5 cm after 10 yr and 10 cm after 20 yr. Thus, we expect to be able to decipher between models

when longer time-series will be available, possibly in 5 yr from now.

This discussion brings another argument in favour of using Burgers rheologies, rather than Maxwell’s or non-Newtonian’s: on one hand a Maxwell rheology does not produce both the decennial transient and the steady-state behaviour. On the other hand, as already discussed by Trubienko *et al.* (2014) for the Tohoku earthquake, non-Newtonian rheologies fail to reproduce the large-scale deformation pattern. As a matter of fact, the moment of the three megathrusts of Banda-Aceh, Maule and Tohoku differ by a factor of 5, but the comparison of their far-field post-seismic deformation, normalized by the respective coseismic, show that viscosities do not differ by a factor of 25, which would be the case for non-Newtonian rheologies ($\eta \propto 1/\sigma_{\text{deviatoric}}^2$). Also, because they yield smaller stresses, such rheologies would predict much smaller deformation than observed on the sides of the rupture zone.

5.2 Presence and origin of low-viscosity areas

Our model suggests the presence of a channel extending from the inferior limit of the seismogenic zone down to 135 km, which raises two questions. The first one is whether its existence is substantiated and whether its effect could be replaced by some afterslip deeper on the fault plane. As a matter of fact, both mechanisms would generate the same surface deformation, as long as the slip is introduced over the same time-span and at similar depths. In the viscous relaxation model, the relaxation is simply proportional to the local deviatoric stress and is thus physically predicted, while the ‘slip’ is imposed without explicit link with the stress induced by the megathrust earthquake. For this reason, we suggest to stick with the more physical and straightforward model where calculated viscous relaxation predicts the correct post-seismic pattern.

The second important question relates to the plausible cause of the low-viscosity in the channel. The shallow part of the channel can be explained by the presence of serpentized mantle with 20–30 per cent serpentization (Peacock & Hyndman 1999; Krawczyk *et al.* 2006; Kawakatsu & Watada 2007) just above the slab

interface. At depth between 70 and 135 km down, it can no longer be due to serpentinization but rather to hydrated mantle (Agard *et al.* 2009). Moreover, in North Chile, Martin *et al.* (2003) highlighted a lower-velocity zone relative to the surrounding mantle, above the slab, going down to at least 160 km. We did not find any clear seismological evidence of such zone in South Chile, but it might be possible that such a layer still exists in the Maule area more or less thick and more or less difficult to image.

5.3 Impact of a Craton in Central Argentina

Our best-fit model, involving combined viscoelastic relaxation and afterslip, predicts more deformation in the centre of Argentina than observed and a subsidence not yet detected in the GPS data. This could be due to the existence of a craton in the area, known as the Rio de la Plata craton, located directly in front of the flat slab zone (30°S). Tomographic studies image a zone of high seismic velocity at 200 km depth that could indicate the remaining of a cratonic lithosphere in this area (Heintz *et al.* 2005; Ritsema *et al.* 2011), west of the Parana flood basalt volcanism consequent to the opening of the Atlantic (Thiede & Vasconcelos 2010). Attempts to explain the origin of the flat slab zone in the area of La Serena (30°S) brought out a mechanism combining trenchward motion of a craton and trench retreat (Manea *et al.* 2012). So, we tested the effect of various mechanical properties and size and location of such a cold, elastic craton on the post-seismic deformation predicted in central Argentina. It appears that the presence of a stiff craton in Central Argentina (between 36 and 38°S and between 62 and 68°W) reduces significantly the predicted horizontal velocities in this area and produces a slight rotation of velocities located directly North and South of it (Supporting Information Fig. S13). It also reduces the vertical deformation in the same area. Different tests show that the thickness of this craton has to be at least 100 km. The presence of this craton allows to fine tune the residual velocities observed in Central Argentina, but the geological evidence for such a craton remains scarce. Thus, we consider this hypothesis simply as a plausible explanation for the small differences between observations and predictions of our model. This hypothesis will be further tested with longer time-series, providing better signal/noise ratio, increasing discrepancies between observation and model prediction, and an increased number of GPS stations included in the processing.

5.4 Insight into the seismic cycle

Understanding the post-seismic deformation opens new perspectives in the understanding of the interseismic phase, since the geometry and the rheological parameters constrained with the first 2 yr of post-seismic deformation following the Maule earthquake clearly demonstrate that the elastic rheology is inappropriate. In the case of Sumatra, purely elastic models based on the elastic backslip assumption, imply the introduction of a rigid micro-plate (the Sunda block) to reproduce the observed interseismic velocity pattern (Simons *et al.* 2007). In contrast, models involving a viscoelastic asthenosphere explain the observed velocity pattern before the earthquake without the need for this independent block motion (Trubienko *et al.* 2013). In the case of the subduction of the Nazca plate, elastic models also need the introduction of a sliver to reproduce the interseismic velocity pattern (Brooks *et al.* 2003; Métois *et al.* 2013; Nocquet *et al.* 2014). In turn, viscoelastic models reproducing the entire seismic cycle may not require the introduction of an independent rigid block and rather impute the gradients of

deformation at rather large distance from the trench to the last stage of the seismic cycle. 20 yr of GPS observations, particularly after mega-earthquakes such as the Maule earthquake, highlight some transitory stage of the plate tectonic, during which the viscous response to such major events propagate through the whole plate, first stretching the plate for several decades, then compressing it back during the ‘interseismic stage’. Consequently, GPS measurements made during any period of time, relatively short compared to the seismic cycle or other present-day indicators of the strain-rate such as earthquake focal mechanisms may not completely reflect long-term ‘geologic’ deformation. Caution needs to be taken especially when dealing with smaller plates (<3000 km) lined up with subduction, capable of producing magnitude 9 earthquakes.

6 CONCLUSIONS

We analyse in this study almost 5 yr of GPS data since the Maule earthquake in order to extract very precisely the post-seismic pattern following the 2010 Maule earthquake. This analysis sheds light on various characteristics of the deformation pattern that had already been observed after the Sumatra-Andaman earthquake (2004) and the Tohoku-Oki earthquake (2011) such as large-scale subsidence and significant horizontal trenchward motion up to 2000 km away from the trench. Yet, the 2010 Chilean earthquake offers, for the first time, the opportunity to quantify post-seismic deformation not only very precisely but also continuously across the continent.

We build a finite element model of the region, based on the first 2 yr of data after the earthquake, which allows us to arbitrate in favour of a combined model of afterslip and viscoelastic relaxation. Our preferred model features relaxation in a 4.75×10^{18} Pa s asthenosphere constrained by the far-field deformation, and in a low-viscosity channel extending down to 135 km depth with viscosities close to 10^{17} Pa s, constrained by the mid-field pattern of both horizontal and vertical deformation. Shallow afterslip appears to last more than 2 yr and is necessary to reproduce the very particular near-field pattern. Because this large amount of slip at shallow depth can account for most of the fast displacements during the first year, even in the far-field, the role of a short timescale (1 yr) transient rheology implying short-term asthenospheric viscosities of the order of some 10^{17} Pa s seems rather limited. On the other hand, although modelled here as a long-term viscosity, we do not know whether the 4.75×10^{18} Pa s obtained for the asthenosphere correspond indeed to a long-term viscosity or to a transient viscosity modelled by a Kelvin–Voigt element with a low relaxed modulus as proposed on the basis of the analysis of the post-seismic deformation inflicted by the 2004 Sumatra earthquake (Satirapod *et al.* 2013). Future work on the longer time-scale response to Maule earthquake and examining the long-term post-seismic response to Valdivia earthquake should help clarifying this point.

ACKNOWLEDGEMENTS

We thank the International (Chilean-German-French) Plate boundary Observatory Chile (IPOC) and LIA ‘Montessus de Ballore’ International Laboratory, the Chilean ‘Centro Sismológico Nacional’ (CSN), The US Tectonics Observatory at Caltech CANTO, Ohio State University CAP projects, and French ‘Institut pour la Recherche et le Développement’ (IRD) for sharing GPS data acquired in Chile, the ‘Instituto Geografico Nacional’ (IGN) for

Argentinian RAMSAC data and the ‘Instituto Brasileiro de Geografia e Estatística’ (IBGE) for Brazilian RBMC data. We warmly thank CSN personnel, and among them M.C. Valderas-Bermejo and I. Ortega-Navarete for the maintenance of our common cGPS network in Chile. This work received partial support from ANR-2011-BS56-017 and ANR-2012-BS06-004 grants of the French ‘Agence Nationale de la Recherche’. We thank the Z-set software development team Zset/Zebulon (8.6) for providing the finite element software used in this study. We finally thank our reviewers, especially Dr Moreno and Prof Bürgmann for their extremely thorough and constructive review.

REFERENCES

- Agard, P., Yamato, P., Jolivet, L. & Burov, E., 2009. Exhumation of oceanic blueschists and eclogites in subduction zones: timing and mechanisms, *Earth-Sci. Rev.*, **92**(1), 53–79.
- Altamimi, Z., Collilieux, X. & Métivier, L., 2011. ITRF2008: an improved solution of the international terrestrial reference frame, *J. Geod.*, **85**(8), 457–473.
- Bai, W., Vigny, C., Ricard, Y. & Froidevaux, C., 1992. On the origin of deviatoric stresses in the lithosphere, *J. geophys. Res.*, **97**(B8), 11 729–11 737.
- Bedford, J. *et al.*, 2013. A high-resolution, time-variable afterslip model for the 2010 Maule Mw = 8.8, Chile megathrust earthquake, *Earth planet. Sci. Lett.*, **383**(0), 26–36.
- Brooks, B.A., Bevis, M., Smalley, R., Kendrick, E., Manceda, R., Lauria, E., Maturana, R. & Araujo, M., 2003. Crustal motion in the Southern Andes (26°–36°S): do the Andes behave like a microplate?, *Geochem. Geophys. Geosyst.*, **4**(10), doi:10.1029/2003GC000505.
- Chlieh, M. *et al.*, 2007. Coseismic slip and afterslip of the great Mw 9.15 Sumatra-Andaman Earthquake of 2004, *Bull. seism. Soc. Am.*, **97**(1A), S152–S173.
- Delouis, B., Nocquet, J.-M. & Vallée, M., 2010. Slip distribution of the February 27, 2010 Mw = 8.8 Maule Earthquake, central Chile, from static and high-rate GPS, InSAR, and broadband teleseismic data, *Geophys. Res. Lett.*, **37**(17), L17305, doi:10.1029/2010GL043899.
- Diao, F., Xiong, X., Wang, R., Zheng, Y., Walter, T.R., Weng, H. & Li, J., 2014. Overlapping post-seismic deformation processes: afterslip and viscoelastic relaxation following the 2011 Mw 9.0 Tohoku (Japan) earthquake, *Geophys. J. Int.*, **196**(1), 218–229.
- Dow, J., Neilan, R. & Rizos, C., 2009. The International GNSS Service in a changing landscape of Global Navigation Satellite Systems, *J. Geod.*, **83**(3–4), 191–198.
- Dziewonski, A.M. & Anderson, D.L., 1981. Preliminary reference earth model, *Phys. Earth planet. Inter.*, **25**(4), 297–356.
- Han, S., Sauber, J. & Pollitz, F., 2014. Broad-scale postseismic gravity change following the 2011 Tohoku-Oki earthquake and implication for deformation by viscoelastic relaxation and afterslip, *Geophys. Res. Lett.*, **41**(16), 5797–5805.
- Hayes, G.P., Wald, D.J. & Johnson, R.L., 2012. Slab1.0: a three-dimensional model of global subduction zone geometries, *J. geophys. Res.*, **117**(B1), doi:10.1029/2011JB008524.
- Heintz, M., Debayle, E. & Vauchez, A., 2005. Upper mantle structure of the South American continent and neighboring oceans from surface wave tomography, *Tectonophysics*, **406**(1–2), 115–139.
- Herring, T., King, R. & McClusky, S.C., 2010. *GLOBK: Global Kalman filter VLBI and GPS analysis program release 10.4*.
- Hsu, Y. *et al.*, 2006. Frictional afterslip following the 2005 Nias-Simeulue Earthquake, Sumatra, *Science*, **312**(5782), 1921–1926.
- Hu, Y. & Wang, K., 2012. Spherical-earth finite element model of short-term postseismic deformation following the 2004 Sumatra earthquake, *J. geophys. Res.*, **117**(B5), doi:10.1029/2012JB009153.
- Hu, Y., Wang, K., He, J., Klotz, J. & Khazaradze, G., 2004. Three-dimensional viscoelastic finite element model for postseismic deformation of the great 1960 Chile earthquake, *J. geophys. Res.*, **109**(B12), B12403, doi:10.1029/2004JB003163.
- Hu, Y., Bürgmann, R., Freymueller, J., Banerjee, P. & Wang, K., 2014. Contributions of poroelastic rebound and a weak volcanic arc to the postseismic deformation of the 2011 Tohoku earthquake, *Earth Planets Space*, **66**(1), doi:10.1186/1880-5981-66-106.
- Jonsson, S., Segall, P., Pedersen, R. & Björnsson, G., 2003. Post-earthquake ground movements correlated to pore-pressure transients, *Nature*, **424**(6945), 179–183.
- Kawakatsu, H. & Watada, S., 2007. Seismic evidence for deep-water transportation in the mantle, *Science*, **316**(5830), 1468–1471.
- Khazaradze, G., Wang, K., Klotz, J., Hu, Y. & He, J., 2002. Prolonged post-seismic deformation of the 1960 great Chile earthquake and implications for mantle rheology, *Geophys. Res. Lett.*, **29**(22), 7-1–7-4.
- King, R. & Bock, Y., 2000. *Documentation for the GAMIT Analysis Software, release 10.0*.
- Klotz, J., Khazaradze, G., Angermann, D., Reigber, C., Perdomo, R. & Cifuentes, O., 2001. Earthquake cycle dominates contemporary crustal deformation in central and southern Andes, *Earth planet. Sci. Lett.*, **193**(3), 437–446.
- Krawczyk, C.M. *et al.*, 2006. Geophysical signatures and active tectonics at the South-Central Chilean margin, in *The Andes, Frontiers in Earth Sciences*, pp. 171–192, eds Oncken, O., Chong, G., Franz, G., Giese, P., Götze, H.-J., Ramos, V., Strecker, M. & Wigger, P., Springer.
- Lange, D. *et al.*, 2012. Aftershock seismicity of the 27 February 2010 Mw 8.8 Maule earthquake rupture zone, *Earth planet. Sci. Lett.*, **317–318**, 413–425.
- Lin, Y.-n.N. *et al.*, 2013. Coseismic and postseismic slip associated with the 2010 Maule Earthquake, Chile: characterizing the Arauco Peninsula barrier effect, *J. geophys. Res.*, **118**(6), 3142–3159.
- Lorito, S. *et al.*, 2011. Limited overlap between the seismic gap and coseismic slip of the great 2010 Chile earthquake, *Nat. Geosci.*, **4**(3), 173–177.
- Manea, V.C., Pérez-Gussinyé, M. & Manea, M., 2012. Chilean flat slab subduction controlled by overriding plate thickness and trench rollback, *Geology*, **40**(1), 35–38.
- Marone, C.J., Scholtz, C.H. & Bilham, R., 1991. On the mechanics of earthquake afterslip, *J. geophys. Res.*, **96**(B5), 8441–8452.
- Martin, S., Rietbrock, A., Haberland, C. & Asch, G., 2003. Guided waves propagating in subducted oceanic crust, *J. geophys. Res.*, **108**(B11), doi:10.1029/2003JB002450.
- Melnick, D., Moreno, M., Motagh, M., Cisternas, M. & Wesson, R., 2012. Splay fault slip during the Mw8.8 2010 Maule Chile earthquake, *Geology*, **40**(3), 251–254.
- Melosh, H.J. & Raefsky, A., 1983. Anelastic response of the Earth to a dip slip earthquake, *J. geophys. Res.*, **88**(B1), 515–526.
- Métouis, M., Vigny, C. & Socquet, A., 2012. Interseismic coupling, segmentation and mechanical behavior of the central Chile subduction zone, *J. geophys. Res.*, **662**, 120–131.
- Métouis, M. *et al.*, 2013. Revisiting the North Chile seismic gap segmentation using GPS-derived interseismic coupling, *Geophys. J. Int.*, **194**(3), 1283–1294.
- Moreno, M. *et al.*, 2011. Heterogeneous plate locking in the south-central Chile subduction zone: building up the next great earthquake, *Earth planet. Sci. Lett.*, **305**, 413–424.
- Moreno, M. *et al.*, 2012. Toward understanding tectonic control on the Mw 8.8 2010 Maule Chile earthquake, *Earth planet. Sci. Lett.*, **321–322**, 152–165.
- Nocquet, J.-M. *et al.*, 2014. Motion of continental slivers and creeping subduction in the northern andes, *Nat. Geosci.*, **7**(4), 287–291.
- Peacock, S.M. & Hyndman, R.D., 1999. Hydrous minerals in the mantle wedge and the maximum depth of subduction thrust earthquakes, *Geophys. Res. Lett.*, **26**(16), 2517–2520.
- Ritsema, J., Deuss, A., van Heijst, H.J. & Woodhouse, J.H., 2011. S40RTS: a degree-40 shear-velocity model for the mantle from new Rayleigh wave dispersion, teleseismic traveltimes and normal-mode splitting function measurements, *Geophys. J. Int.*, **184**(3), 1223–1236.

- Ruegg, J. *et al.*, 2009. Interseismic strain accumulation measured by GPS in the seismic gap between Constitución and Concepción in Chile, *Phys. Earth planet. Inter.*, **175**, 78–85.
- Ruiz, J.A., Hayes, G.P., Carrizo, D., Kanamori, H., Socquet, A. & Comte, D., 2014. Seismological analyses of the 2010 March 11, Pichilemu, Chile Mw 7.0 and Mw 6.9 coastal intraplate earthquakes, *197*(1), 414–434.
- Ruiz, S. *et al.*, 2013. The Constitución earthquake of 25 March 2012: a large aftershock of the Maule earthquake near the bottom of the seismogenic zone, *Earth planet. Sci. Lett.*, **377–378**(0), 347–357.
- Ryder, I., Rietbrock, A., Kelson, K., Bürgmann, R., Floyd, M., Socquet, A., Vigny, C. & Carrizo, D., 2012. Large extensional aftershocks in the continental forearc triggered by the 2010 Maule earthquake, Chile, *Geophys. J. Int.*, **188**(3), 879–890.
- Satirapod, C., Trisirisatayawong, I., Fleitout, L., Garaud, J. & Simons, W., 2013. Vertical motions in Thailand after the 2004 Sumatra – Andaman earthquake from GPS observations and its geophysical modelling, *Adv. Space Res.*, **51**(8), 1565–1571.
- Savage, J.C., 1983. A dislocation model of strain accumulation and release at a subduction zone, *J. geophys. Res.*, **88**(B6), 4984–4996.
- Simons, W. *et al.*, 2007. A decade of GPS in Southeast Asia: resolving Sundaland motion and boundaries, *J. geophys. Res.*, **112**(B6), doi:10.1029/2005JB003868.
- Suito, H. & Freymueller, J.T., 2009. A viscoelastic and afterslip postseismic deformation model for the 1964 Alaska earthquake, *J. geophys. Res.*, **114**(B11), doi:10.1029/2008JB005954.
- Sun, T. & Wang, K., 2015. Viscoelastic relaxation following subduction earthquakes and its effects on afterslip determination, *J. geophys. Res.*, **120**, 1329–1344.
- Thatcher, W. & Rundle, J.B., 1984. A viscoelastic coupling model for the cyclic deformation due to periodically repeated earthquakes at subduction zones, *J. geophys. Res.*, **89**(B9), 7631–7640.
- Thiede, D.S. & Vasconcelos, P.M., 2010. Paraná flood basalts: rapid extrusion hypothesis confirmed by new $^{40}\text{Ar}/^{39}\text{Ar}$ results, *Geology*, **38**(8), 747–750.
- Tong, X. *et al.*, 2010. The 2010 Maule, Chile earthquake: downdip rupture limit revealed by space geodesy, *Geophys. Res. Lett.*, **37**(24), L24311, doi:10.1029/2010GL045805.
- Trubienko, O., 2013. Interseismic and postseismic deformations and the seismic cycle associated with large subduction earthquakes, *PhD thesis*, Laboratoire de géologie, ENS, Paris.
- Trubienko, O., Fleitout, L., Garaud, J.-D. & Vigny, C., 2013. Interpretation of interseismic deformations and the seismic cycle associated with large subduction earthquakes, *Tectonophysics*, **589**(0), 126–141.
- Trubienko, O., Garaud, J.-D. & Fleitout, L., 2014. Models of postseismic deformation after megathrust earthquakes: the role of various rheological and geometrical parameters of the subduction zone, *Solid Earth Discuss.*, **6**(1), 427–466.
- Vargas, G., Farias, M., Carretier, S., Tassara, A., Baize, S. & Melnick, D., 2011. Coastal uplift and tsunami effects associated to the 2010 Mw8.8 Maule earthquake in Central Chile, *Andean Geol.*, **38**, 219–238.
- Vigny, C., Rudloff, A., Ruegg, J.C., Madariaga, R., Campos, J. & Alvarez, M., 2009. Upper plate deformation measured by GPS in the Coquimbo Gap, Chile, *Phys. Earth planet. Inter.*, **175**(1), 86–95.
- Vigny, C. *et al.*, 2011. The 2010 Mw 8.8 Maule Megathrust Earthquake of Central Chile, monitored by GPS, *Science*, **332**(6036), 1417–1421.
- Yamagiwa, S., Miyazaki, S., Hirahara, K. & Fukahata, Y., 2015. Afterslip and viscoelastic relaxation following the 2011 Tohoku-oki earthquake (Mw9.0) inferred from inland GPS and seafloor GPS/Acoustic data, *Geophys. Res. Lett.*, **42**, 66–73.
- Yue, H., Lay, T., Rivera, L., An, C., Vigny, C., Tong, X. & Baez Soto, J., 2014. Localized fault slip to the trench in the 2010 Maule Chile Mw8.8 earthquake from joint inversion of high-rate GPS, teleseismic body waves, InSAR, campaign GPS, and tsunami observations, *J. geophys. Res.*, **119**, doi:10.1029/2010GL045805.
- Zienkiewicz, O. & Taylor, R., 2000. *The Finite Element Method: Solid Mechanics*, Vol. 2, Butterworth-Heinemann.
- Zset/Zebulon, 8.6. *Material and structure analysis suite*, <http://www.zset-software.com/>.

SUPPORTING INFORMATION

Additional Supporting Information may be found in the online version of this paper:

Table S1. Stations used for the realization of the global reference frame.

Table S2. Shear (G in Pa) and Bulk (K in Pa) moduli as function of depth (PREM).

Table S3. Correlation matrix of the viscous parameters inversion.

Figure S1. Interseismic velocity field across the whole area expressed in ITRF08 (International Terrestrial Reference Frame). Blue vectors represent the measured velocities, the red ones are interpolated using cubic spline.

Figure S2. Analysis process of GPS time series, here on the east component of the station of Maule, MAUL, at different stage of the analysis. Insert map shows the location of the station (black diamond) and the Maule earthquake epicenter, from CSN (red star). (a) Complete raw time serie. Estimated interseismic velocity is represented by the black line. (b) Complete time series corrected from the interseismic velocity previously estimated. (c) Postseismic time series, the global trend is represented in black, annual mean velocities are represented in blue.

Figure S3. 3D Finite Element mesh featuring a portion of a spherical shell from the core-mantle boundary to the Earth's surface, extending over 60° in longitude and latitude. On the right is represented the planar top surface of the mesh, colours defining the different layers and white lines highlight the elements of the mesh. On the bottom is the slab, colours are function of the depth, white lines represent the elements.

Figure S4. Sketches of the tested rheologies: A. Maxwell rheology; B. Simple Burgers rheology (one Kelvin-Voigt element); C. Complex Burgers with two Kelvin-Voigt elements.

Figure S5. (a) Coseismic slip distribution inverted in this study, origin of data are detailed above. The red star depicts the hypocentre (CSN); (b) Residuals (Observed versus Computed) in horizontal (red) and in vertical (blue); Observed (blue) versus predicted (red) coseismic displacements (in m) of the earthquake on GPS stations (a) in horizontal and (b) in vertical.

Figure S6. Effect on surface velocities of relaxation in the low viscosity wedge (in addition to Fig. 5): (a) Amplitude of horizontal velocities (Ampl Vh in mm yr^{-1}); (b) Vertical velocities (Vup in mm yr^{-1}).

Figure S7. Horizontal evolution as function of time, of the model of pure viscoelastic relaxation on a grid of 1 degree.

Figure S8. Observed versus predicted mean velocities (mm yr^{-1}) between 2011.2 and 2012.2, in the case of the model of pure viscoelastic relaxation in the region of Coquimbo-La Serena (North of the Maulea area).

Figure S9. Observed versus predicted mean velocities (mm yr^{-1}) between 2011.2 and 2012.2, in the case of 2 models of pure viscoelastic relaxation: the preferred model with undissociated asthenosphere (blue) and a model with different viscosities attributed to the continental (4.75×10^{18} Pa s - inverted value) and oceanic (1×10^{20} Pa s) sides of the asthenosphere (green); Horizontal (up), vertical (down).

Figure S10. Observed versus predicted mean velocities (mm yr^{-1}) between 2010.2 and 2011.2, in the case of the preferred combined model of viscoelastic relaxation and afterslip: left) horizontal velocities, right) vertical velocities. The slip distribution of afterslip is represented in colour scale (in m).

Figure S11. Sample of GPS time series (red) compared to the preferred model of viscoelastic relaxation combined to afterslip (green). Grey dashed lines mark known dates of material changes. Stations are located on the map.

Figure S12. Partial derivative of the computed velocities with respect to the viscosities of the reference model in (a) the asthenosphere (amplitude of horizontal velocities mm yr^{-1}); (b) the shallow channel (amplitude of horizontal velocities mm yr^{-1} down to 105 km); (c) in the shallow channel (Vertical velocities mm yr^{-1}); (d) in the deep extension of the deep channel (Vertical velocities mm yr^{-1} , down to 135 km).

Figure S13. Impact of an elastic craton in central Argentina on horizontal deformation over the 2nd year after the earthquake in surface: (top) Zoom over Central Argentina : Observed (red) versus

predicted horizontal velocities (mm yr^{-1}) of the preferred model without craton (blue) and the same model with a craton (green); (bottom) Profile of horizontal velocities (mm yr^{-1}) as function of distance from the trench. Dots represent horizontal velocities (mm yr^{-1}) measured at GPS stations, red dots are GPS stations located on the map b, around and over the craton along the profiles. The 2 lines represent the models with (solid lines) and without craton (dashed lines), along the profiles A (blue) and B (black) (<http://gji.oxfordjournals.org/lookup/suppl/doi:10.1093/gji/ggw086/-/DC1>).

Please note: Oxford University Press is not responsible for the content or functionality of any supporting materials supplied by the authors. Any queries (other than missing material) should be directed to the corresponding author for the paper.